Wave-current interactions at the Tagus Estuary Mouth (Portugal) under storm wave conditions

Baptiste Mengual, Xavier Bertin, Florian Place, Marc Pezerat, Thibault Coulombier, Diogo Mendes, André Bustorff Fortunato

Journal Pre-proof

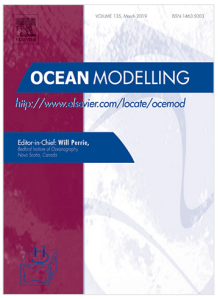

Wave-current interactions at the Tagus Estuary Mouth (Portugal) under storm wave conditions

Baptiste Mengual, Xavier Bertin, Florian Place, Marc Pezerat, Thibault Coulombier, Diogo Mendes, André Bustorff Fortunato

PII: S1463-5003(22)00067-1
DOI: https://doi.org/10.1016/j.ocemod.2022.102035
Reference: OCEMOD 102035

To appear in: *Ocean Modelling*

Received date : 29 January 2022
Revised date : 19 May 2022
Accepted date : 20 May 2022

Please cite this article as: B. Mengual, X. Bertin, F. Place et al., Wave-current interactions at the Tagus Estuary Mouth (Portugal) under storm wave conditions. *Ocean Modelling* (2022), doi: https://doi.org/10.1016/j.ocemod.2022.102035.

Wave-current interactions at the Tagus Estuary Mouth (Portugal) under storm wave conditions

Baptiste Mengual[1,2,*], Xavier Bertin[1,*], Florian Place[1], Marc Pezerat[1], Thibault Coulombier[1], Diogo Mendes[3], André Bustorff Fortunato[4]

[1] UMR 7266 LIENSs CNRS-La Rochelle Université, 2 rue Olympe de Gouges, La Rochelle, France.

[2] now at SAS Benoit Waeles–Consultant Génie Côtier, 53 rue du Commandant Groix, 29200 Brest, France.

[3] HAEDES, Casais do Arrocho, 2025-452 Azóia de Cima, Santarém, Portugal.

[4] National Laboratory for Civil Engineering, Av. do Brasil, 101, Lisbon, Portugal.

Corresponding authors: Baptiste Mengual (baptiste.mengual@bw-cgc.fr) ; Xavier Bertin (xavier.bertin@univ-lr.fr).

Abstract

This study investigates interactions between waves, water levels and currents at the mouth of the second largest estuary in Europe (the Tagus Estuary, Portugal) under storm waves, combining field observations and a three-dimensional fully coupled wave-current modelling system. Tidal-induced water depth variations substantially modulate waves over the ebb shoal. During energetic conditions, low tide levels promote depth-limited wave breaking and energy transfer towards higher harmonics (triad interactions), which reduces wave heights and periods. Furthermore, for a given water level, tidal currents also influence wave propagation and drive strong modulations over shallow regions characterized by cross-channel current gradients. Flood currents change the mean wave direction by about 10-15° and tend to focus the wave energy flux towards coastal regions of the southern margin compared to a run without currents (20 to 30% increase of wave heights), while ebb currents reduce the wave heights. In addition, model results suggest that the saturation level associated with wave and current conditions at shallow locations may be close to the threshold where waves start to dissipate by whitecapping. At the peak of the storm, waves become a main driver of the circulation at the mouth scale, even in the 45-m deep main channel. Wave breaking acceleration over the ebb-shoal locally increases flood currents by 50 to 300% and reduces ebb currents by 20 to 50%.

Keywords: Wave-current interactions; storm waves; large estuary mouth; the Tagus Estuary.

1. Introduction

Inlets and estuaries concentrate many socio-economic and environmental issues such as the maintenance of navigation channels, the stability of adjacent coasts and the flooding of low-lying areas under extreme events, or the water quality and hydrologic characteristics which are crucial for the biodiversity. These natural systems are generally subject to the overlap of several forcings like waves, tide, wind and river discharge, which interact over complex bathymetries characterized by the presence of channels and shoals. Understanding the impact of wave-current interactions (WCI) in these environments is crucial to provide accurate predictions of waves, which largely influence or contribute to storm surges and coastal inundation (e.g. Bertin et al., 2015; Fortunato et al., 2017), navigation hazards (e.g. Zippel and Thomson, 2017), water quality and nutrient exchanges (e.g. Delpey et al., 2014; Chen et al., 2019), or sediment transport and morphodynamics (e.g. Bertin et al., 2009; Dodet et al., 2013; Fortunato et al., 2021).

WCI have been widely studied for several decades using various approaches including analytical solutions (Phillips, 1977), field observations (e.g. Wolf and Prandle, 1999; Wargula et al., 2014; Zippel and Thomson, 2017), laboratory experiments (e.g. Chawla and Kirby, 2002), phase-resolving models (e.g. Chen and Zou, 2018), or numerical modelling systems coupling a circulation model with a spectral wave model (e.g. Bertin et al., 2009; Olabarrieta et al., 2011; Dodet et al., 2013; Akan et al., 2017). Such modelling systems constitute valuable tools to discriminate and analyze separately the hydrodynamic effect of different physical processes, with less expensive computational times than phase-resolving models. Therefore, phase-averaged spectral wave models have been largely used to investigate WCI. While many modeling studies were performed by investigating separately the respective effects of waves on the mean circulation

and the effects of depth-averaged circulations on wave fields (e.g. Smith and Smith, 2001; Kang and Di Iorio, 2006; Rusu et al., 2011), fully coupled wave-current models have been successfully applied to realistic coastal environments in the last two decades (e.g. Bertin et al., 2009; Olabarrieta et al. 2011; Dodet et al., 2013; Akan et al., 2017; Chen et al., 2015, 2019; Lin et al., 2021). In addition, the coupling between waves and currents in 3D was the subject of several theoretical works in this period (e.g. Mellor, 2003; Ardhuin et al., 2008). Uchiyama et al. (2010) and Bennis et al. (2011) proposed a practical framework based on a vortex force formalism, which allows to simulate realistically the depth-varying mean circulation in coastal areas such as beaches (Kumar et al., 2012; Guérin et al., 2018) and, more rarely, tidal inlets (e.g. Olabarrieta et al., 2011).

Previous studies on WCI highlighted that water level changes caused by tidal oscillations superimposed on bathymetric effects strongly influence wave propagation and dissipation at the mouth of inlets or estuaries, in particular due to the presence of ebb delta shoals, which promote wave breaking and thus reduce wave heights landward (Smith and Smith, 2001; Kang and Di Iorio, 2006; Olabarrieta et al., 2011; Chen et al., 2015). Furthermore, waves can be affected by currents in different manners. Ebb currents generally promote shoaling and wave steepening, which increase wave heights by 20% to 80% (e.g. Rusu et al., 2011; Dodet et al., 2013). Depending on the magnitude and the vertical shear of the flow, wave steepening can exceed a threshold and opposed currents can dissipate wave energy by whitecapping (e.g. Dodet et al., 2013; Jia et al., 2015; Akan et al., 2017; Zippel and Thomson, 2017). For shallow depths, ebb currents can even lead to partial or total wave blocking (Dodet et al., 2013; Bertin et al., 2019). On the contrary, flood currents generally reduce wave heights due to de-shoaling (e.g. Rusu et al., 2011; Jia et al., 2015; Mendes et al., 2020). The modulation of wave fields can also occur through current-induced refraction and Doppler shift effect (e.g. Wolf and Prandle, 1999; Bolaños et al., 2014). Conversely, waves may influence circulations through different mechanisms such as the Stokes drift, wave forces and in particular wave breaking-induced acceleration (e.g. Olabarrieta et al., 2011; Chen et al., 2015), enhanced surface mixing through the injection of turbulent kinetic energy caused by wave breaking (e.g. Zippel and Thomson, 2015), or enhanced-bottom stress (e.g. Olabarrieta et al., 2011; Lin et al., 2021).

However, the literature on wave-current interactions (WCI) under storm wave conditions remains scarce, especially for large inlets like the Tagus Estuary Mouth (TEM). Most studies were conducted under low to moderate energy wave conditions while a few showed that WCI can be particularly relevant under storm waves (e.g. Bolaños et al., 2014; Bertin et al., 2015; Chen et al., 2015; Fortunato et al., 2017; Chen et al., 2019). This can be partly explained by the difficulty to deploy and recover instruments in nearshore regions in presence of energetic waves. Consequently, the ability of numerical models to reproduce hydrodynamics and WCI during extreme events is not fully established. In addition, applications generally deal with small to medium-size inlets, with very few studies focusing on large estuary mouths. In this context, this study aims to investigate WCI at the TEM, the second largest estuary in Europe, combining field observations and the application of a 3D fully coupled wave-current modelling system, during a period characterized by storm waves.

The paper is organized as follows. Section 2 presents the main characteristics of the Tagus Estuary, the field campaign and data processing. The numerical modelling system is described in Section 3. Section 4 describes wave conditions during the campaign period and the model validation at measuring stations. Interactions between waves, water levels, and currents are described in Section

5, while key points provided by this study regarding wave-current interactions are discussed in Section 6. Finally, the main conclusions are summarized in Section 7.

2. Study area and field campaign

2.1. Description of the study site

The Tagus Estuary, located on the west coast of Portugal, is the second largest estuary in Europe with a surface area of around 320 km^2. This estuary is bordered by a metropolitan area of about 2 million inhabitants and combines many socio-economic challenges such as water quality, the presence of low-lying zones or the stability of the urbanised southern margin. The Atlantic Ocean is connected to a shallow tide-dominated basin through a 45 m-deep, 10 km-long and 2 km-wide tidal inlet cut into the bedrock (Figure 1). The continental shelf width is about 40 km in front of the TEM.

The TEM is a semi-diurnal meso-tidal environment characterised by tidal ranges varying from 0.55 m to 3.86 m at the coast (Guerreiro et al., 2015), and by a strong dominance of the ebb with currents reaching up to 2.5 m/s (Fortunato et al., 1999). The average discharge of the Tagus River is 336 m^3/s, but can reach 2000 to 4000 m^3/s in the winter (Costa et al., 2007; Rodrigues and Fortunato, 2017), and even occasionally exceeds 10000 m^3/s (Salgueiro et al., 2013). The estuary is generally well-mixed given the low average river flow, but it can become partially mixed and even stratified when the river flow intensifies, in particular during neap tides (Neves, 2010; Rodrigues and Fortunato, 2017).

The wave regime is dominated by long-period swells generated in the North Atlantic Ocean. During the winter, offshore mean wave conditions correspond to significant wave heights of 2.5 m, peak periods of 12.1 s and a mean wave direction of 305° (Dodet et al., 2010; Mendes and Oliveira, 2021). Due to the Roca Cape to the northwest, the estuary mouth is partly sheltered from waves originating from the prevailing northwest direction but is fully exposed to waves coming from the southwest and the west, which can reach significant heights of 10 m during extreme storms (Fortunato et al., 2017).

At the mouth, complex bed morphologies are found over ebb shoals, like the Bugio Bank (Figure 1b), with bed sediments mainly composed of marine medium sands (Freire et al., 2007). For the past eight decades, the morphology of the TEM has been experiencing a significant evolution, in particular a strong erosion of the ebb shoal and the adjoining beaches (Fortunato et al., 2021).

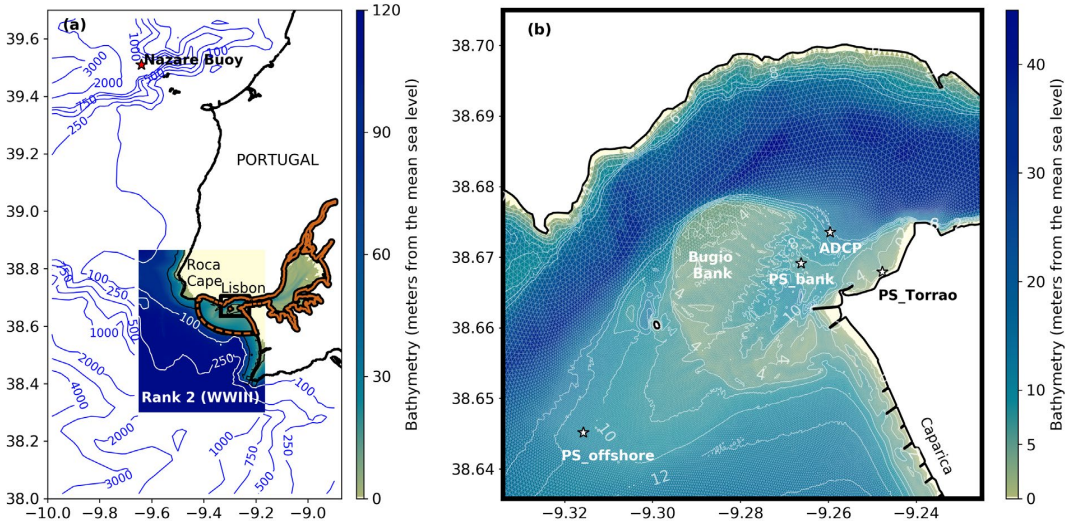

Figure 1. (a) Bathymetric contours (blue isobaths) associated with the large-scale rank of the wave model WaveWatchIII (WWIII), on which is superimposed the extent and the bathymetry of the second WWIII rank (Rank 2), forced by the large-scale rank along its open boundary. On (a), the brown contour delimits the SCHISM-WWM unstructured grid forced at its open boundary (dotted line) by wave spectra from Rank 2. **(b)** Zoom over the TEM for the SCHISM-WWM configuration, with its bathymetry, the locations of measuring stations (white stars), the computational grid, and isobaths (contours every 2 m from 0 to 14 m).

2.2. Field campaign and data processing

Three RBR™ pressure sensors and one 600 kHz Nortek ADCP (Acoustic Doppler Current Profiler) mounted with a pressure sensor were deployed at the TEM during one week (from the 16th to 24th November, 2019), during which offshore wave heights (H_{m0}) and peak periods (T_p) reached 6 m and 20 s, respectively (Figure 2). From offshore to nearshore locations (Figure 1b), sensors PS_offshore (-9.316; 38.645), PS_bank (-9.266; 38.67) and PS_Torrao (-9.247; 38.668) were respectively deployed at mean water depths of 10.6 m, 5.9 m and 3 m (Figure 1b). PS_offshore and PS_bank were fixed to anchors directly deployed on the seabed whereas PS_Torrao was fixed on a pillar, at 1.65 m above the seabed. The station PS_Torrao is located at the beach of the neighbourhood of Segundo Torrão, frequently subject to damages and inundations during storms. Continuous pressure measurements were made at a sampling frequency of 2 Hz. The ADCP (-9.26; 38.673; mean water depth of 10.24 m), was set in an upward-looking position with 0.50 m-thick cells, providing average current profiles every 30 minutes and 20-minute bursts of pressure measurements every hour (at 2 Hz). Unfortunately, ADCP measurements are only available over the first 1.5 days of the field campaign, due to a malicious act.

To compute wave bulk parameters, pressure time series recorded at PS_offshore, PS_bank and PS_Torrao were split into 1 hour-long bursts, corrected from atmospheric pressure and tidal

oscillations. The tidal signal was removed by applying a low-pass filter with a 1-hour window and pressure was converted to water depth under a hydrostatic assumption. Power density spectra associated to frequencies f were computed by applying a Fast Fourier Transform and by considering 10 Hanning-windowed segments (with an overlap of 50%), which results in 17 equivalent degrees of freedom with a frequency resolution of 0.003 Hz. Note that the number of equivalent degrees of freedom was estimated from the power spectral density, and was then reduced by 10% (specific to the case with 10 segments) according to the procedure described by Elgar (1987). Then, the elevation spectra were reconstructed using the Transfer Function Method based on the linear wave theory (TFM; e.g. Bishop and Donelan, 1987) at the three stations, PS_offshore, PS_bank and PS_Torrao. The TFM involves wave numbers, computed from the linear dispersion relation, which is affected by the presence of ambient currents. The current effect was considered in the calculation of the wave number using currents simulated by the numerical model at each pressure sensor location, with a similar strategy as de Wit et al. (2019). The procedure is described in Appendix A. To avoid noise amplification, the TFM method requires the definition of an upper cut-off frequency, f_{max}, which was set to 0.3 Hz for all pressure sensors (in agreement with Inch et al., 2017). From each spectrum, wave parameters can be computed using the *i-th* moments, m_i, as follows

$$m_i = \int_{f_{min}}^{f_{max}} f^i E(f)\, df \qquad (1)$$

The integration of the spectral energy in Eq. (1) requires the definition of a lower cut-off frequency, f_{min}, in order to separate the energy band associated with short waves from the one of infragravity waves. According to the literature, f_{min} can be expressed as a function of the peak frequency, f_p, which corresponds to the frequency where the maximum energy is found in the gravity band (e.g. Roelvink and Stive, 1989; Oh et al., 2020). Following Roelvink and Stive (1989), who defined this lower cut-off frequency as half the peak frequency, f_{min} is computed here as

$$f_{min} = \max\{\, 0.036\, Hz; \min\{0.5 \times\ f_p; 0.05\, Hz\}\} \qquad (2)$$

In Eq. (2), f_p is firstly computed between 0.04 and 0.3 Hz, and then updated according to the new f_{min} estimate. Although a fixed cut-off frequency is employed in most studies, an adaptive approach was required here as the incident peak period ranged from 6 and 20 s during the studied period. Finally, the significant wave height, H_{m0}, and the mean wave period, T_{m02}, are computed as follows

$$H_{m0} = 4\sqrt{m_0} \qquad (3)$$

$$T_{m02} = \sqrt{\frac{m_0}{m_2}} \qquad (4)$$

In order to integrate bulk wave parameters within the same band and ensure consistent comparisons between sensors, f_{min} series computed at PS_offshore were applied to PS_bank and PS_Torrao.

3. The numerical modelling system

The modelling system is based on the full coupling, at the source code level, between the third-generation spectral wave model Wind Wave Model of Roland et al. (2012, hereafter WWM), and the hydrodynamic core based on the Semi-Implicit Cross-scale Hydroscience Integrated System Model (hereafter SCHISM) of Zhang et al. (2016). Both models share the same unstructured grid and domain decomposition.

3.1. Spectral wave model - WWM

WWM simulates surface gravity waves generation, propagation and dissipation by solving the wave action equation (Komen et al., 1994) that reads:

$$\frac{\partial N}{\partial t} + \nabla_{\boldsymbol{x}}.(\dot{\boldsymbol{x}}N) + \frac{\partial(\dot{\sigma}N)}{\partial\sigma} + \frac{\partial(\dot{\theta}N)}{\partial\theta} = \frac{1}{\sigma}(S_{in} + S_{nl4} + S_{nl3} + S_{ds} + S_{br} + S_{bf}) \qquad (5)$$

where t is the time, σ is the relative wave frequency (=$2\pi f$, with f the wave frequency), θ is the wave direction, N is the wave action (=$\frac{E(\sigma,\theta)}{\sigma}$, $E(\sigma,\theta)$ being the discrete variance density of the sea level elevation), $\nabla_{\boldsymbol{x}}$ is the horizontal gradient operator, and $\dot{\boldsymbol{x}}$, $\dot{\sigma}$, and $\dot{\theta}$ are the propagation velocities in space, frequency and direction, respectively.

WWM accounts for water depths and currents fields obtained from SCHISM, with $\dot{\boldsymbol{x}} = \boldsymbol{C_g} + \tilde{\boldsymbol{u}}$ in Eq. (5), $\boldsymbol{C_g}$ being the wave group velocity vector (=$c_g(\cos\theta, \sin\theta)$, with c_g the wave group velocity computed from the linear wave theory). The advection velocities in the different phase spaces include the effect of a "wave-weighted" current field $\tilde{\boldsymbol{u}} = (\tilde{u}, \tilde{v})$ that is computed according to Kirby and Chen (1989), which enables to consider the circulation over a surface layer where waves are assumed to be kinematically active. The right-hand side of Eq. (5) details all the source terms, which correspond to the wind input (S_{in}), the nonlinear interaction in deep and shallow water (S_{nl4} and S_{nl3}, respectively), the energy dissipation due to whitecapping (S_{ds}), depth-limited breaking (S_{br}) and bottom friction (S_{bf}).

The nonlinear energy transfer in deep water (quads), S_{nl4}, is approximated using the Discrete Interaction Approximation following Hasselmann and Hasselmann (1985). The nonlinear energy transfer in shallow water (triads), S_{nl3}, has been prescribed following the Lump Triad Approximation introduced by Eldeberky (1996; equation 7.25), using a parameter α adjusted to 0.35, which is consistent with the range of values proposed by the author. Both terms linked to

wind input (S_{in}) and dissipation due to whitecapping (S_{ds}) follow Ardhuin et al. (2010). The S_{ds} term is defined as

$$S_{ds}(\sigma,\theta) = \sigma \frac{C_{ds}^{sat}}{B_r(\sigma)^2}(\max\{B(\sigma,\theta) - B_r(\sigma)\,;0\}^2)N(\sigma,\theta) + S_{bk,cu} + S_{turb} \quad (6)$$

where C_{ds}^{sat} is a nondimensional constant of 2×10^{-4}, $B_r(\sigma)$ is a threshold, and $B(\sigma,\theta)$ is the nondimensional energy level at each frequency and direction, also called saturation, which is defined as

$$B(\sigma,\theta) = \int_{\theta-\Delta_\theta}^{\theta+\Delta_\theta} k^3 \cos^{s_B}(\theta-\theta')E(\sigma,\theta')\frac{C_g}{2\pi}d\theta' \quad (7)$$

with k the mean wave number, and s_B a constant set to 2. In Ardhuin et al. (2010), the threshold for the saturation B_r is a constant (9×10^{-4}). A directional width, $\Delta_\theta = 80°$, is introduced in the saturation computation in order to account for different dissipation rates in the different directions. In Eq. (6), the term S_{turb} refers to wave-turbulence interactions (Ardhuin and Jenkins, 2006) and $S_{bk,cu}$ is a cumulative breaking term that represents the smoothing of small waves by big breakers (Ardhuin et al., 2009).

However, the sensitivity of model results to the S_{ds} term will be further discussed by testing an alternative formulation. More specifically, the latter was modified in order to mimic observations showing pronounced energy dissipation in the high frequency part of spectra when waves faced intense and opposed currents. A dependency of the saturation B_r threshold on the frequency, f, is introduced such as

$$B_r(\sigma) = (B_{r,LF} - B_{r,HF}) \times e^{C_{br}\cdot(f_{cr}-f)} + B_{r,HF} \quad (8)$$

In Eq. (8), $B_{r,LF}$ is the reference saturation threshold of 9×10^{-4} proposed by Ardhuin et al. (2010), which is, in this case, associated with low frequencies. It is assumed that for frequencies larger than f_{cr}, B_r decreases exponentially, at a rate controlled by the parameter C_{br}, towards a reduced value, $B_{r,HF}$, associated with high frequencies (HF). This modification has been introduced as model/data comparison revealed a local underestimation of dissipation by whitecapping in the model, which will be discussed later. Values of f_{cr}, C_{br}, and $B_{r,HF}$ tested to assess the model sensitivity to the dissipation by whitecapping are detailed in section 3.4.

The energy dissipation due to depth-limited wave breaking, S_{br}, is computed according to the model of Baldock et al. (1998), as corrected by Janssen and Battjes (2007), and by using the breaking index formulation of Ruessink et al. (2003), which is a function of the dimensionless depth $k_p.h$, k_p being the peak wave number and h the water depth.

Lastly, the wave dissipation by bottom friction, S_{bf}, is computed in agreement with the empirical model of Hasselmann et al. (1973) based on the JONSWAP experiments, with a dissipation coefficient of 0.038 $m^2.s^{-3}$, which is adequate for swell waves.

3.2. Hydrodynamic model - SCHISM

SCHISM, which evolved from SELFE (Zhang and Baptista, 2008), solves the 3D Reynolds-averaged Navier-Stokes equations under hydrostatic and Boussinesq assumptions on unstructured grids. SCHISM uses an Eulerian-Lagrangian Method combined to semi-implicit schemes to treat the advection term in momentum equations, which relaxes the numerical stability constraints and allows using large time steps (CFL numbers larger than one). Wave force terms are included in the momentum equations in order to account for 3D wave-induced circulations. Wave forces are computed following the vortex-force (VF) formalism as described by Bennis et al. (2011). The VF implementation in SCHISM is described in Guérin et al. (2018). Wave-induced breaking momentum is concentrated in the two upper layers below the surface, as proposed by Bennis et al. (2011).

Regarding turbulence, the model uses a closure based on the Generic Length Scale (GLS) turbulence model of Umlauf and Burchard (2003), in a $k-\varepsilon$ configuration (Rodi, 1993). At the boundaries, the turbulent kinetic energy (*TKE*) and the mixing length (l) are specified as Dirichlet boundary conditions, and account for wave-enhanced turbulence. At the surface, the *TKE* is defined by accounting for both wind stress (Pond and Pickard, 1998) and vertical mixing due to wave breaking (Moghimi et al., 2013). According to Feddersen (2012), 15% of the energy dissipated by wave breaking is effectively transformed into *TKE*. The length scale associated with the surface wave-enhanced turbulence is defined as a function of a surface roughness set to $0.6\times H_{m0}$ (Terray et al., 1996).

The wind stress is also used as a boundary condition for the internal Reynolds stress at the surface. At the bottom, the Reynolds stress is prescribed through a bottom stress that combines the effects of waves and currents (Soulsby, 1997), assuming a roughness length z_0 of 5×10^{-4} m, which was the best compromise to reproduce vertical profiles of currents at the ADCP location (Section 4.2).

3.3. The Tagus Estuary configuration

The unstructured grid used for the Tagus Estuary is characterized by a spatial resolution varying from 500 m at its offshore open boundary to 25 m over shallow parts of the Bugio Bank and along adjacent beaches within surf zones (Figure 1). For the vertical discretization, 21 S-levels are considered with a refinement in upper and lower parts of the water column ($\theta_b = 1$ and $\theta_f = 3$ in the formulation of Song and Haidvogel (1994)). Both hydrodynamic and wave models use the same time step, here set to 10 s.

The tidal forcing is computed considering 21 constituents from the global tide model FES2014 (Lyard et al., 2021), linearly interpolated along the open boundary. The atmospheric forcing originates from the Climate Forecast System Reanalysis (CFSR; Saha et al., 2014) with temporal and spatial resolutions of 3 hours and 0.2°, respectively. CFSR winds and atmospheric pressure series were compared against observations at the Nazaré Buoy (longitude=-9.54; latitude=39.51; depth=2000 m; location on Figure 1a). The accuracy of atmospheric reanalyses is characterized with the root mean square discrepancy (RMSD), the normalized RMSD (NRMSD), and the bias (BIAS). The wind speed is on average well predicted with a normalized root mean square discrepancy (hereinafter NRMSD) of 21.6%. Given weak river runoffs during our field campaign (average of 80 m^3/s; maximum of 146 m^3/s; source: https://snirh.apambiente.pt/), river discharge and baroclinic effects associated with temperature and salinity were neglected in numerical simulations. The spectral wave forcing originates from a 2-rank structured and nested configuration of the WaveWatchIII (WWIII) spectral wave model, forced by CFSR winds described above. The WWIII configuration is based on the *TEST471* (Ardhuin et al., 2010; WW3DG, 2019). The first rank covers the North Atlantic with a 20-km resolution. The second rank, forced at its open boundaries by the first one, encompasses the entire estuary bay with a 500 m resolution, in order to reproduce wave refraction around the Roca Cape (Figure 1). Both WWIII ranks use a spectral discretization of 36 frequencies (0.036 to 1 Hz) and 48 directions. At the Nazaré Buoy, significant wave heights and peak periods computed from WWIII show a very good agreement with the observations, with NRMSD of 8% and 13%, respectively (Figure 2). Finally, spectra from the second WWIII rank are interpolated along the open boundary of the SCHISM-WWM grid, and WWM is run by considering 24 frequencies ranging from 0.036 and 0.4 Hz, and 24 directions.

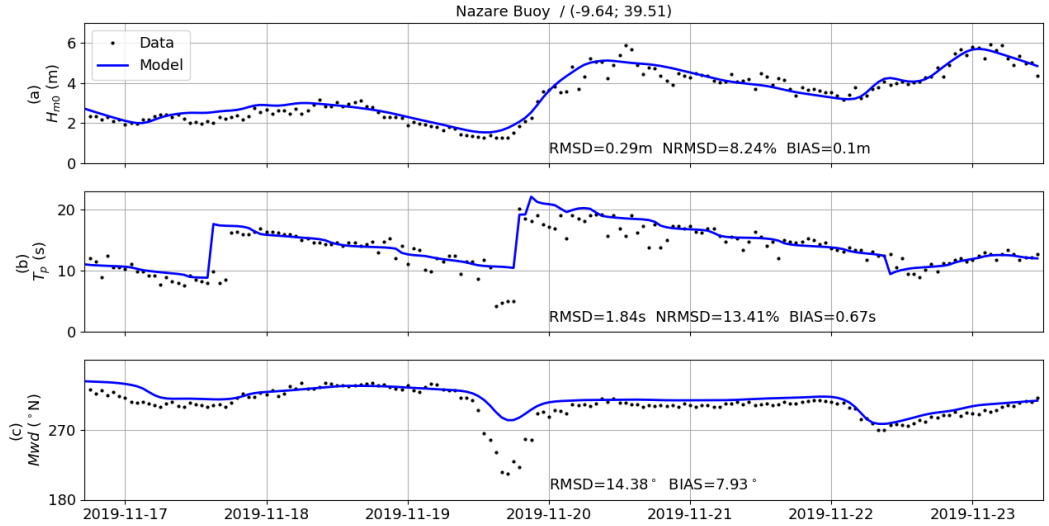

Figure 2. Comparisons between observed (black dots) and modelled wave parameters (thick solid line) at the Nazaré Buoy (see location on Figure 1a): **(a)** significant wave height H_{m0}, **(b)** mean wave period T_{m02}, and **(c)** mean wave direction *Mwd*. Model predictions are computed with the WaveWatchIII model (Rank 1).

3.4. Numerical experiment

Wave transformations and wave-current interactions have been investigated through a set of 6 simulations. The reference simulation, *Ref*, considers a full coupling between hydrodynamic and wave models and includes all the physics of waves (i.e. all source terms), as described in section 3.1. To investigate the tidal modulation of waves obtained from *Ref*, two simulations are considered in the following analysis: *Run 2* only includes variations of tide levels without current effects on waves, and *Run 3* does not account for the effect of both water level oscillations and currents on waves. In order to evaluate the importance of wave-induced circulations in *Ref*, wave forces were ignored in the hydrodynamic model SCHISM in the simulation *Run 4*. Further simulations are dedicated to sensitivity analyses. First, while a constant saturation threshold B_r is assumed in the whitecapping dissipation term in *Ref* (9×10^{-4}, as suggested by Ardhuin et al. (2010)), an adaptive saturation threshold is considered in another simulation, *Run 5*, assuming an exponential decrease towards high frequencies (C_{br}=30) from $B_{r,LF}=9\times10^{-4}$ to $B_{r,HF}=9\times10^{-5}$ beyond the frequency f_{cr}=0.2 Hz (Eq. 8). Moreover, the implication of triad wave interactions on wave transformations was quantified by turning off the S_{nl3} term (Eq. 5) in simulation *Run 6*. Model configurations for the 6 numerical simulations are summarized in Table 1.

Simulation	Current effect on waves?	Water level effect on waves?	Wave forces?	Adaptive whitecapping threshold?	Wave triads (S_{nl3})?
Ref	Yes	Yes	Yes	No	Yes
Run 2	No	Yes	Yes	No	Yes
Run 3	No	No	Yes	No	Yes
Run 4	Yes	Yes	No	No	Yes
Run 5	Yes	Yes	Yes	Yes	Yes
Run 6	Yes	Yes	Yes	No	No

Table 1. Model configurations for the 6 numerical simulations.

4. Wave conditions and model validation at sensor locations

The model validation is described here for the reference simulation, *Ref* (see Section 3.4), in terms of water levels, wave bulk parameters and depth-dependent currents. A more thorough analysis of model results is then provided in section 5.

4.1. Water levels and wave bulk parameters

Water levels are well reproduced by the model at PS_offshore, PS_bank and PS_Torrao, with NRMSD (RMSD normalized by the mean tidal range) of 3%, 4%, and 2.5%, respectively.

At PS_offshore (Figure 3), measured significant wave heights, H_{m0}, vary between 0.5 and 1.5 m during the first half of the period ("calm" period) and then increase substantially during stormy conditions and reach 3.65 m. Wave heights are generally well reproduced by the model with a NRMSD of 15%. Nevertheless, the model tends to slightly overestimate H_{m0} during "calm periods" (< 1.5 m), and peaks occurring at low tide under energetic wave conditions (> 2 m) are not reproduced. Mean wave periods, T_{m02}, obtained from pressure measurements range between 5 and 8 s during calm periods and between 8 and 10 s during the storm. T_{m02} periods are well reproduced overall by the model with a NRMSD of 14%, despite a persistent bias of 0.7 s over the period. The discrete peak period, T_p, reaches up to 20 s during the storm and is well reproduced by the model with a NRMSD of 20% and a weak positive bias of 0.5 s. In more details, this larger error compared to other bulk parameters is mostly due to the presence of a bimodal sea state on the 17th November where the local wind sea is underestimated by the model. If this period is discarded, the NRSMD drops to 12%.

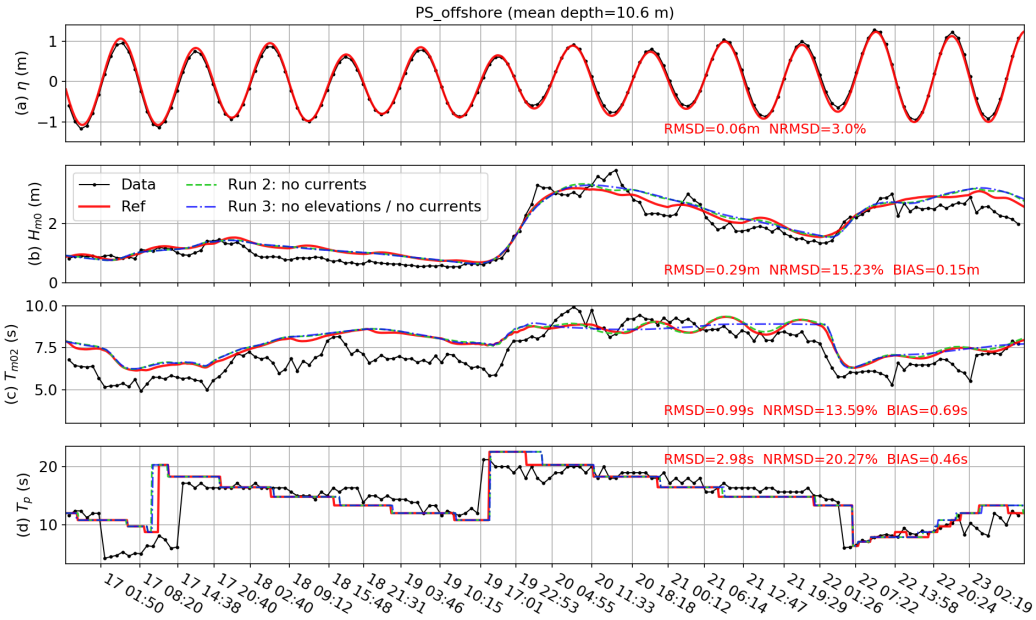

Figure 3. Comparisons of sea surface elevation (**a**), significant wave height H_{m0} (**b**), mean wave period T_{m02} (**c**) and wave peak period T_p (**d**) at PS_offshore station (see location on Figure 1b) between data and model results from simulations *Ref*, *Run 2* (no currents) and *Run 3* (no elevations and no currents). RMSD, NRMSD and BIAS values indicated on each subplot refer to simulation *Ref*.

At PS_bank (Figure 4), measured wave heights range between 0.5 and 0.8 m during the calm period, and between 0.8 and 1.8 m during energetic conditions. Wave heights are strongly tidally-modulated, with a minimum at low tide and fluctuations ranging from 0.25 m to 1 m. Modelled H_{m0} are reproduced with a NRMSD of 14%, with a good ability to capture tidal modulations, despite a slight but persistent underestimation on flood during energetic conditions. Tidal-induced modulations of measured T_{m02} are also substantial (around +/- 1.5 s) with values ranging between 5 and 10 s. Modelled T_{m02} are well reproduced with a NRMSD of 10%, in spite of weaker tidal-induced fluctuations leading to both under- and over-estimations throughout the period.

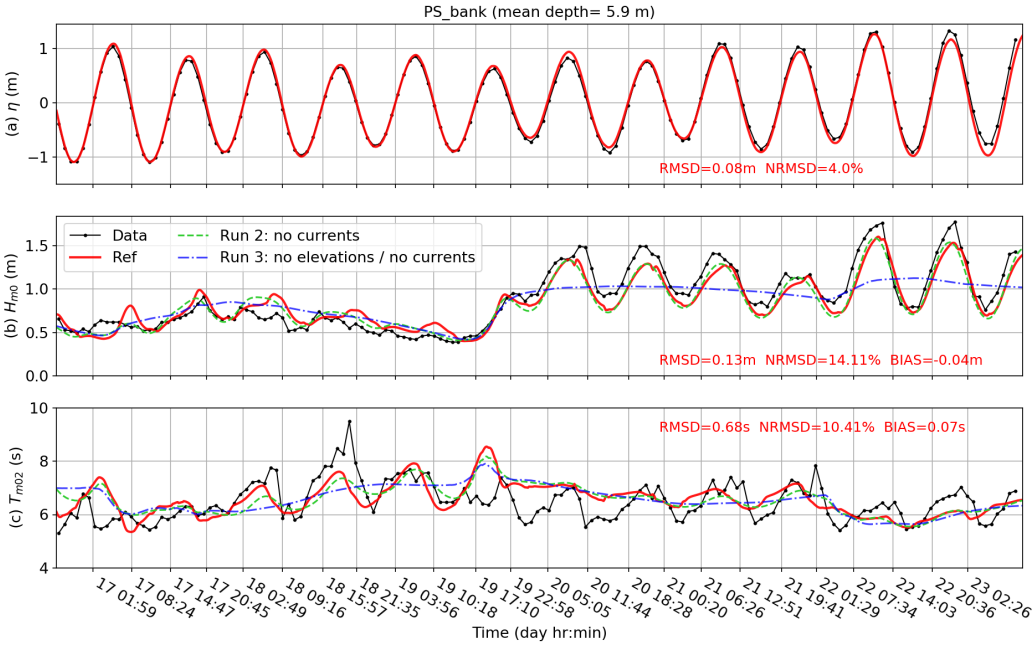

Figure 4. Comparisons of sea surface elevation (**a**), significant wave height H_{m0} (**b**), and mean wave period T_{m02} (**c**) at PS_bank station (see location on Figure 1b) between data and model results from simulations *Ref*, *Run 2* (no currents) and *Run 3* (no elevations and no currents). RMSD, NRMSD and BIAS values indicated on each subplot refer to simulation *Ref*.

Finally, at PS_Torrao station (Figure 5), similar fluctuations as at PS_bank are observed for wave heights and periods. Due to its more sheltered location, wave heights are comprised between 0.25 and 0.5 m during the calm period and reach up to 1.25 m throughout the campaign period. H_{m0} values are well reproduced by the model with a NRMSD of 16%. Regarding wave periods, measured T_{m02} range between 6 and 9 s and are reproduced by the model with a NRMSD of 9%, although the model tends to underestimate the drop in wave period at low tide as in PS_bank.

The discrete peak period T_p does not exhibit significant spatio-temporal variations in comparisons with the mean period T_{m02}. T_p values obtained at PS_bank and PS_Torrao appear very close to those at PS_offshore, and are thus omitted here. At these two shallow stations, T_p is reproduced by the model with a NRMSD of about 15%.

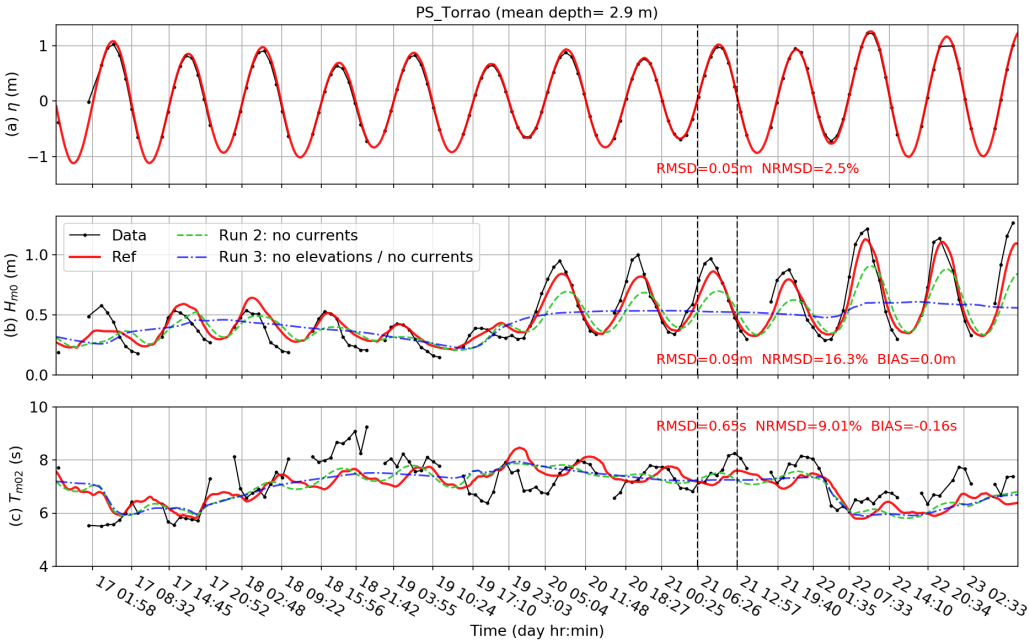

Figure 5. Comparisons of sea surface elevation (**a**), significant wave height H_{m0} (**b**), and mean wave period T_{m02} (**c**) at PS_Torrao station (see location on Figure 1b) between data and model results from simulations *Ref*, *Run 2* (no currents) and *Run 3* (no elevations and no currents). RMSD, NRMSD and BIAS values indicated on each subplot refer to simulation *Ref*. Thicker vertical ticks refer to specific dates used in the following analyses.

4.2. Currents

At 1 meter above the bed, both zonal (U) and meridional (V) components of currents data from the ADCP are well reproduced by the model with NRMSD values of 25% and 32%, respectively (Figure 6b,c). Maximum currents occur during the flood and the ebb, with average magnitudes of 0.54 m/s and 0.67 m/s, respectively. The current flows towards the east-northeast during the flood and reverses during the ebb towards the west-southwest. At 8 m above the bed, the current direction is similar but its magnitude is around 30% higher (Figure 6d,e). Like near the seabed, the current is about 25% higher on ebb than on flood, with average values of 0.9 m/s and 0.7 m/s, respectively. At the surface, the model tends to overestimate the duration of maximum current phase associated with the flood for both components, resulting in a generally weaker agreement with observations (NRMSD of about 35%).

Focusing on vertical profiles of currents at mid-flood and mid-ebb times (Figure 7), the agreement between observations and model results is generally good. NRMSD values range between 4.6% and 20.3% at mid-flood, and between 2.4% and 7.3% at mid-ebb.

Although no measurements were available during this period, the comparison between our reference run and a simulation without wave forces suggests important differences during

energetic wave conditions (from the 19th of November at 22:50), with flood currents increased by 30% close to the surface.

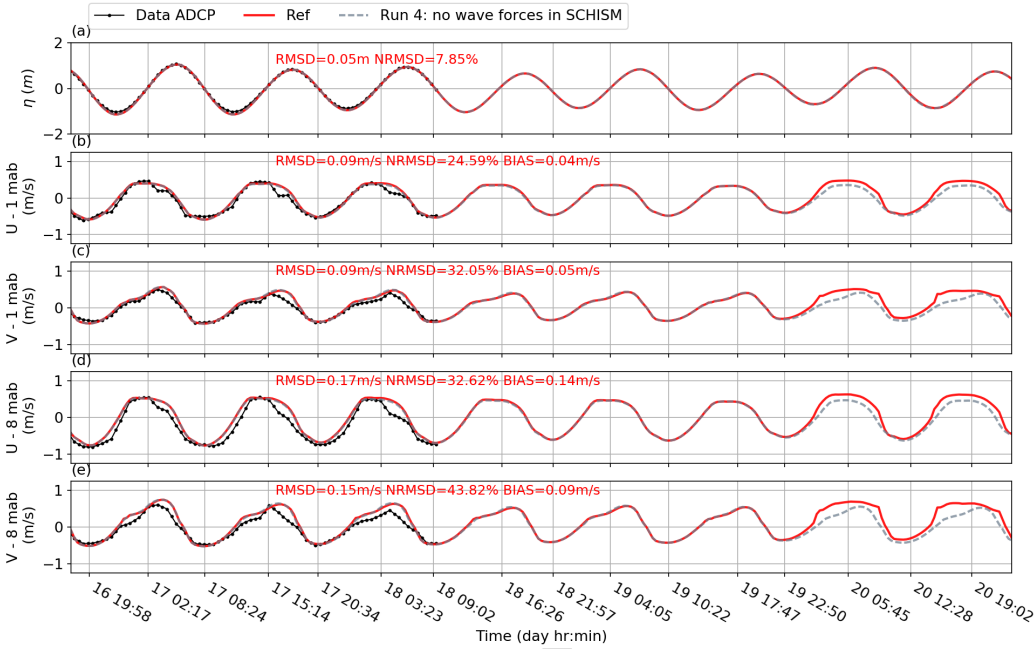

Figure 6. Comparisons of ADCP data and model results from simulations *Ref* and *Run 4* (no wave forces in SCHISM) in terms of sea surface elevation (**a**; around mean sea level), and zonal (*U*) and meridional (*V*) components of currents at 1 m above the bed (on **b** and **c**, respectively) and 8 m above the bed (on **d** and **e**, respectively). Statistical parameters RMSD, NRMSD and BIAS refer to the *Ref* accuracy with respect to observations.

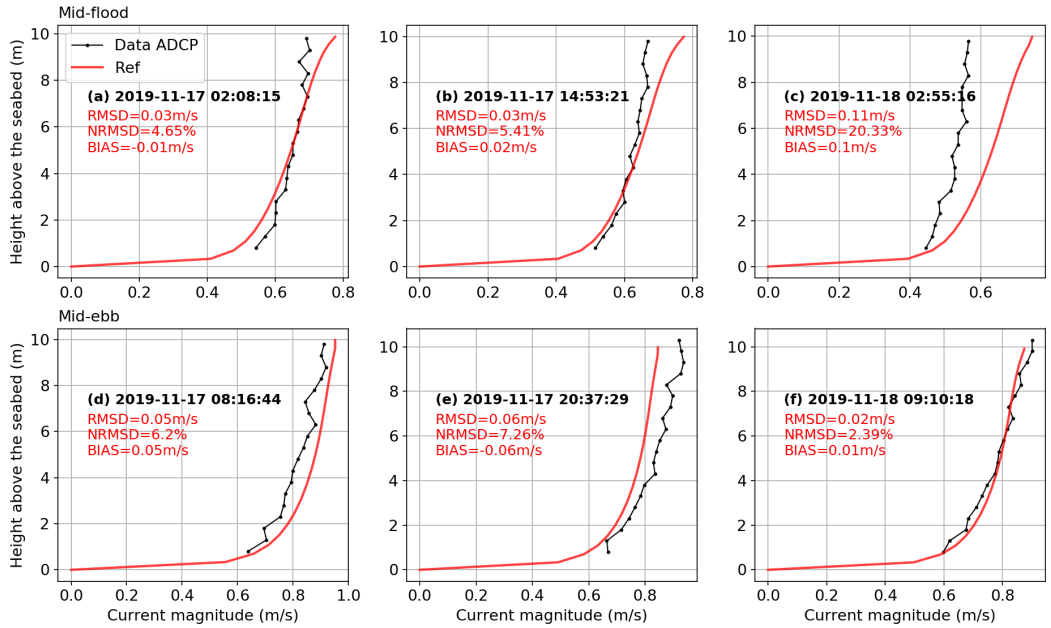

Figure 7. Comparisons of vertical profiles of currents (magnitude) obtained from the ADCP data and model results from simulation *Ref*, at 3 mid-flood (from **a** to **c**) and 3 mid-ebb situations (from **d** to **f**). Statistical parameters RMSD, NRMSD and BIAS refer to the *Ref* accuracy with respect to observations.

5. Analysis of wave-tide-current interactions

The wave modulations caused by the tide are assessed through a comparison between *Ref* (reference physical setting and full coupling between SCHISM and WWM), *Run 2* (no currents in WWM), and *Run 3* (no elevations and no currents in WWM). Regarding model predictions from the reference run *Ref*, two simulations are included hereafter in order to discuss the importance of wave energy dissipation caused by whitecapping (*Run 5* with an adaptive saturation threshold B_r in Eq. 8), and of wave triad interactions (*Run 6* without triads).

5.1. Impact of water level variations on short waves

5.1.1. Wave heights

At PS_offshore, both observed and modelled wave heights only exhibit a very limited tidal modulation by water levels during calm periods because of its large water depth (10 m), as highlighted by the similarity between results obtained from *Run 2* and *Run 3* (Figure 3b).

At the shallower station PS_bank, the tidal signature on H_{m0} is different, with, to first order, a positive correlation between H_{m0} and the water depth. Focusing on high tide (HT) and low tide (LT) situations, when currents are the weakest, data provide evidence for larger *Hm0* (+54%) during HT (Figure 4). Including water level variations without currents in the wave model (*Run 2*) enables to reproduce this modulation of H_{m0} between LT and HT, which is completely missed otherwise (*Run 3*). In addition, similarities between model results from *Ref* and *Run 2* on Figure 4 suggest that wave modulations are mostly controlled by changes in water levels, with only minor effects of currents. In *Ref*, H_{m0} at HT are 58% higher than at LT.

At PS_Torrao, similar patterns can be observed for H_{m0} with even more pronounced trends: observed and modelled (simulation *Run 2* without current effects) H_{m0} at HT are 157% and 92% higher than at LT, respectively. However, as highlighted by the differences between *Run 2* and *Ref* results, a substantial part of the modulation is due to currents at this location. In *Ref*, H_{m0} at HT are 130% higher than at LT, which is closer to the observed ratio. This behaviour will be further examined in section 5.2.

The distributions of wave heights provided by the model (*Ref*) throughout the period of interest are illustrated along a section crossing the Bugio Bank roughly in the alignment of measurement stations (Figure 8). The major role played by water level changes on depth-limited wave breaking and subsequent H_{m0} modulations is clearly highlighted. During the energetic period, H_{m0} at HT suffers a substantial decrease of 30% at the southwest edge of the ebb delta when the water depth is about 4 m (around X=3000 m on subplots (a) and (c) of Figure 8). At LT, the breaking point is shifted a few hundred metres offshore (i.e. towards PS_offshore) and the H_{m0} decrease is very pronounced over the same region and reaches up to 75%. Therefore, the height of waves propagating over the Bugio Bank at HT is on average 50% higher than at LT. In addition, H_{m0} at LT never exceeds 0.75 m at the coast.

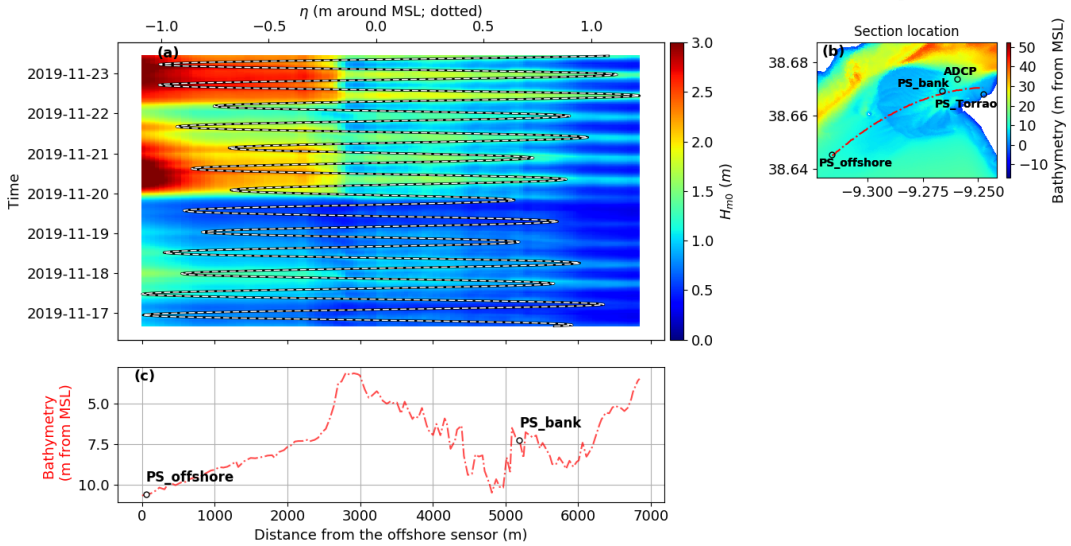

Figure 8. (a) Spatio-temporal variations of significant wave heights, H_{m0} (m), computed from simulation *Ref* along a section crossing the Bugio Bank and fitting the sensor positions (black circles) and the mean direction of waves, as shown on **(b)**. On **(a)** temporal variations of sea surface elevation are superimposed (white dashed line; top abscissa axis). The bathymetry along the section is illustrated on (c).

5.1.2. Wave periods

Coherently with H_{m0} variations, observed wave periods do not exhibit significant tidal modulations at PS_offshore during calm periods (Figure 3c,d). Only small T_{m02} differences correlated with tidal levels are highlighted by the model during the energetic period. Modelled T_{m02} at HT are between 5 and 10% higher than at LT in *Run 2* accounting for tide elevations, which is not the case in *Run 3*.

At PS_bank, a pronounced tidal modulation of wave periods is observed. Focusing on HT/LT differences, measured T_{m02} are on average 18% larger at HT (Figure 4c). By accounting for water level changes in WWM (*Run 2*), the model is able to reproduce a part of the tidal modulation with T_{m02} at HT around 7% higher than at LT.

At PS_Torrao, the sensor was generally not submerged at LT, making it difficult to highlight clear trends compared to the HT situation based on observations. However, coherently with PS_bank, measured T_{m02} are on average 8% higher at HT (Figure 5c). Modelled T_{m02} at HT are only 3% higher than at LT in *Run 2*.

During the energetic period (between the 20th and the 22nd November), measured wave periods T_{m02} decrease from PS_offshore to PS_bank (or PS_Torrao). Model results highlight that this trend can only be reproduced by considering triad wave interactions, which result in nonlinear energy transfers from low to high frequencies. Indeed, triad wave interactions are usually identified as a

key mechanism for energy transfers between wave frequencies in the nearshore region, that may cause substantial changes in wave characteristics (e.g. Elgar and Guza, 1985; Beji and Battjes, 1993; Herbers et al., 2000; Rusu and Soares, 2011; Cavaleri et al., 2018).

T_{m02} computed from run *Run 6*, that ignores triads, are almost similar at the three sensor locations and display a strong positive bias compared to the observations (not illustrated here). Focusing on a LT situation during the energetic period (the 20th November at 3 pm), the wave spectrum derived from bottom pressure observation at PS_offshore provides evidence for this type of energy transfer with successive peaks obtained at f_p (peak frequency) and $2\times f_p$ (Figure 9a). While *Ref* mimics the spectrum shape with the different energy peaks, *Run 6* misses this trend and strongly overestimates T_{m02} (by 70%). At PS_bank, the energy remains concentrated in the frequency band lower than 0.1 Hz in *Run 6* with a T_{m02} of 14.4 s, whereas the energy becomes more distributed over frequencies in data and *Ref* with T_{m02} values of 5.7 s and 6.7 s, respectively (Figure 9b). Note that energy is also transferred to the third harmonic in observations ($3\times f_p$), which is not reproduced by the model in simulation *Ref*. This is further discussed in section 6.1.

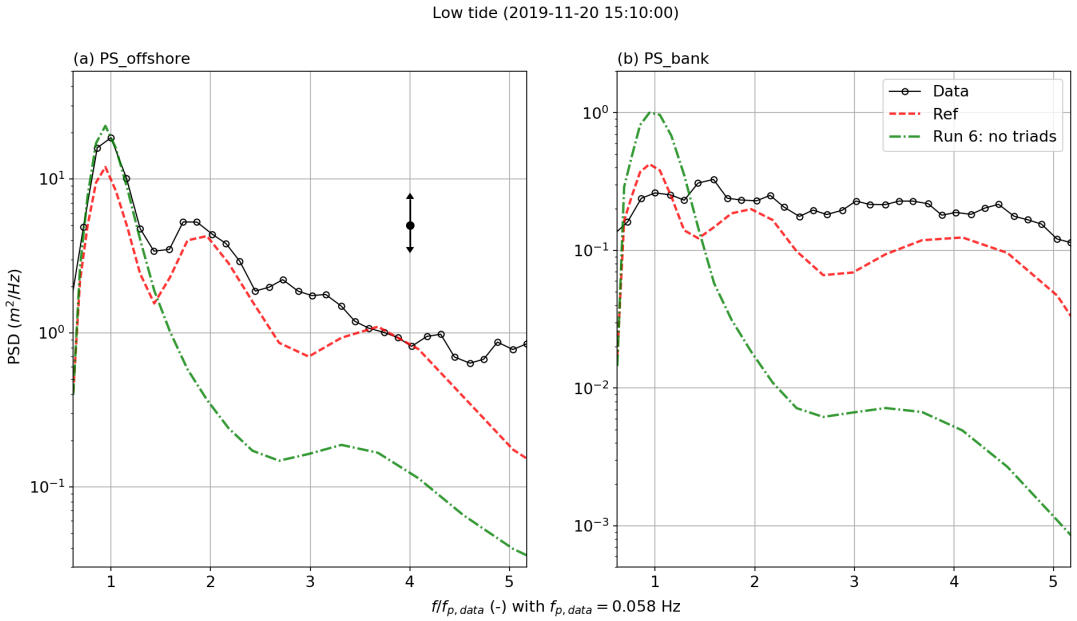

Figure 9. Power spectral density (PSD) as a function of normalized frequency (by $f_{p,data}$=0.058 Hz) obtained from pressure measurements, and simulations *Ref* and *Run 6* at PS_offshore **(a)** and PS_bank **(b)** during a low tide situation occurring at the storm peak (the 20th of November at 3:10pm). On (a), the error bar refers to the 95% interval of confidence of the PSD (Bendat and Piersol, 1971).

5.2. Impact of currents on the wave field

The offshore location of PS_offshore only shows a slight influence of currents on wave parameters during the energetic period, with differences of only a few percent for wave heights and periods (weak differences between *Ref* and *Run 2* on Figure 3b, 3c).

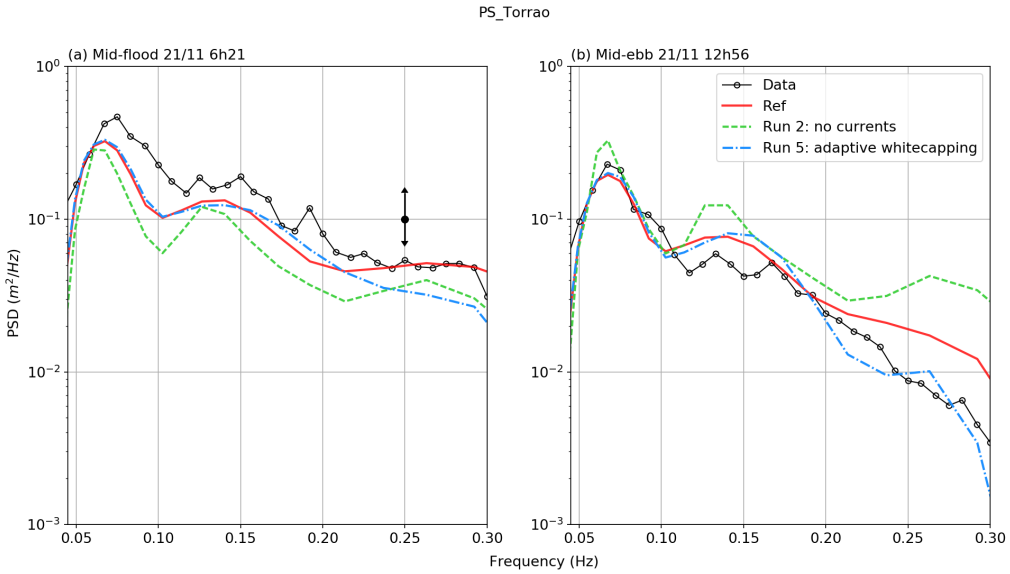

Figure 10. Power spectral density (PSD) obtained from pressure measurements, and simulations *Ref*, *Run 2 (no currents)* and *Run 5 (adaptive whitecapping)* at PS_Torrao during successive mid-flood **(a)** and mid-ebb **(b)** situations, the 21st of November at 6:21 and 12:56, respectively (see the corresponding thick vertical ticks on Figure 5).

Focusing on successive mid-flood (MF) and mid-ebb (ME) situations for equivalent water depths enables to assess the influence of currents on wave heights and periods at the shallower locations. At PS_bank, observations do not provide evidence for a clear effect of currents on H_{m0} and T_{m02} when comparing successive MF and ME situations (Figure 4).

At PS_Torrao, observations reveal that at MF, on average, H_{m0} are 78% higher, and T_{m02} are 11% lower than at ME (Figure 5). In simulation *Ref*, H_{m0} and T_{m02} at MF are 31% higher and 7% lower than at ME, respectively, thus in agreement with observations. Neglecting currents in *Run 2* leads to similar H_{m0} and T_{m02} between MF and ME, and to substantial underestimations by 15-25% of maximum H_{m0} occurring over tidal cycles during the energetic period. Wave spectra obtained from observations and simulations *Ref* and *Run 2* at PS_Torrao clearly highlight the substantial underestimation of the wave energy in the model when currents are neglected, in particular during

589 the flood (Figure 10a). Therefore, substantial current-induced modulations of wave parameters are
590 superimposed on those controlled by water level changes.
591 To understand the processes responsible for these current-induced modulations, spatial fields of
592 wave heights and directions were compared between simulations *Run 2* (without currents) and *Ref*
593 (with currents) during two successive MF and ME situations characterized by similar offshore
594 wave conditions (Figure 11). In *Ref*, flood currents enhance refraction and induce a clockwise
595 rotation of waves of 10-15° in comparison with the simulation *Run 2*, over the region between
596 PS_bank and PS_Torrao (Figure 11g). Consequently, more wave energy is focused towards
597 PS_Torrao, with wave heights in *Ref* 19% higher than in *Run 2* at mid-flood (Figure 11c,e). Note
598 that this energy focusing reaches its maximum at the end of the flood, with waves heights 25 to
599 30% higher in the simulation accounting for currents (*Ref*). In contrast, ebb currents induce a
600 counterclockwise rotation of waves of 10° (differences between *Ref* and *Run 2* on Figure 11h), and
601 reduce the wave energy reaching the region around PS_Torrao. Thus, H_{m0} computed from *Ref* at
602 PS_Torrao is 16% lower than in *Run 2* at ME (Figure 11d,f).
603

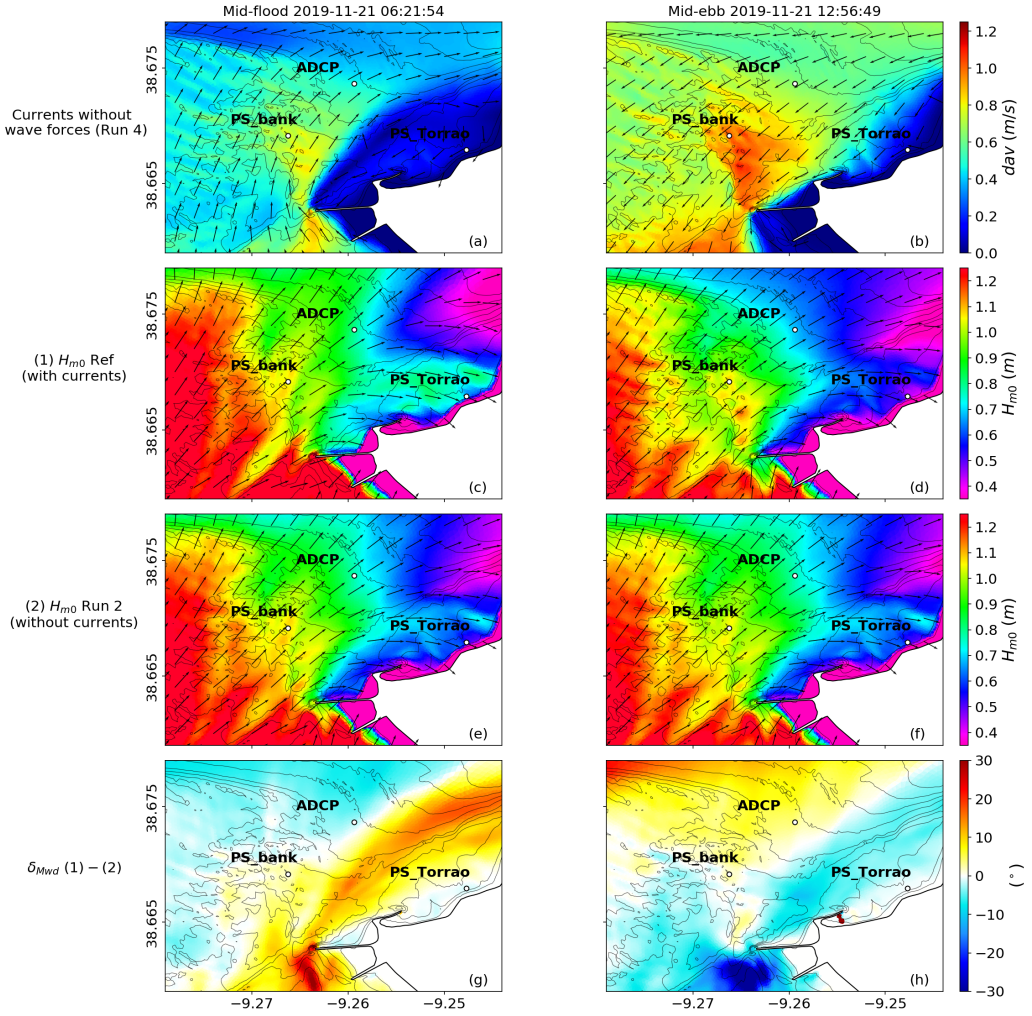

Figure 11. Spatial distributions of depth-averaged currents, *dav*, at successive mid-flood **(a)** and mid-ebb **(b)** situations during the storm peak and the corresponding fields of significant wave height, H_{m0}, from simulations (1) *Ref* (with currents) and (2) *Run 2* (without currents) at mid-flood, (on **(c)** and **(e)**, respectively), and at mid-ebb, (on **(d)** and **(f)**, respectively) (see the corresponding thick vertical ticks associated with these specific dates on Figure 5). Changes in the mean wave direction between *Run 2* and *Ref* (1-2) are illustrated at mid-flood and mid-ebb on **(g)** and **(h)**, respectively.

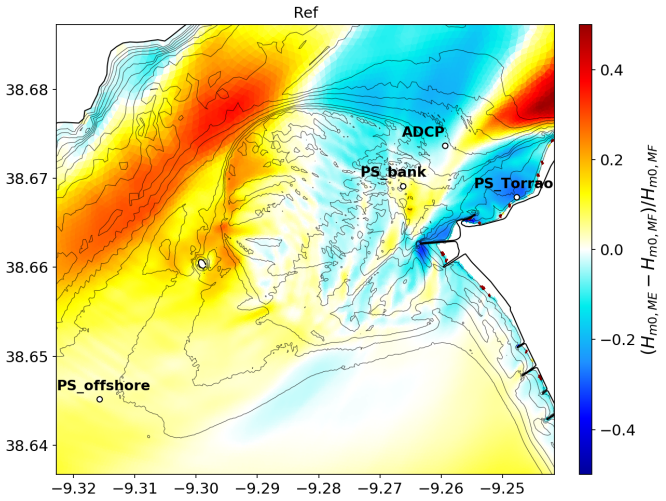

Figure 12. Increasing/decreasing trends of the significant wave height, H_{m0}, between two successive mid-flood (MF, 20th November at 5:02am) and mid-ebb (ME, 20th November at 11:46am) situations during the storm peak, obtained from simulation *Ref.* Trends are expressed as $(H_{m0,ME}\text{-}H_{m0,MF})/H_{m0,MF}$, a positive value meaning that H_{m0} increases at ME, and vice versa.

At a broader extent, circulations affect wave characteristics at the mouth scale, in particular H_{m0}, with different effects depending on the location (current exposure, water depth, sheltered areas and wave dissipation level). Figure 12 illustrates that the H_{m0} decrease occurring between MF and ME is not specific to the station PS_Torrao but concerns large areas of the TEM. Indeed, over the eastern part of the bank, H_{m0} is generally 10 to 40% lower during the ebb. To our knowledge, such a modulation of waves due to current effects on their propagation has never been described at the mouth of a large estuary. This aspect is further discussed in section 6.2. Besides, H_{m0} at ME are not smaller than at MF over the entire mouth. In deeper areas like in the main channel, opposed currents during the ebb promote shoaling without increasing wave steepness enough to induce dissipation by whitecapping. As a result, H_{m0} during ME are about 20-25% higher than during MF over these regions, which corroborates previous findings at the TEM (Rusu et al., 2011) or for other inlet systems (e.g. Elias et al., 2012; Dodet et al., 2013; Jia et al., 2015; Akan et al., 2017). In addition, as already reported in other studies (e.g. Olabarrieta et al., 2011; Dodet et al., 2013; Akan et al., 2017), our results suggest that the strong wave focusing effect of the ebb jet in the main channel induces a redirection of wave energy from adjacent regions, where wave heights thus appear reduced during the ebb. Note that previous studies dedicated to interactions between waves and large-scale currents highlighted that pronounced wave height modulations could be induced by currents in jet area through reflection, refraction or trapping phenomena depending on their orientation with respect to wave directions (e.g. cases of the Agulhas current or the Gulf Steam; see Irvine (1987), Holthuijsen and Tolman (1991), Kudryavtsev et al. (1995), Lavrenov (1998)). In particular, when currents are opposed to waves direction, trapping effect can lead to a

substantial focusing of wave energy in the jet region (mostly resulting from refraction of waves by currents). By using a third-generation spectral wave model, Holthuijsen and Tolman (1991) highlighted this phenomenon in the Gulf Stream region. Over the deep channel area, model results during the energetic peak of the period show that ebb currents tend to induce an anticlockwise rotation of wave directions (by a few degrees) to the west of the Bugio Bank (comparison between H_{m0} fields of simulations *Ref* and *Run 2* without current effects on waves; not illustrated here). This slight refraction of waves at the main channel entrance focuses wave energy in the jet area during the ebb.

5.3. Impact of waves on currents

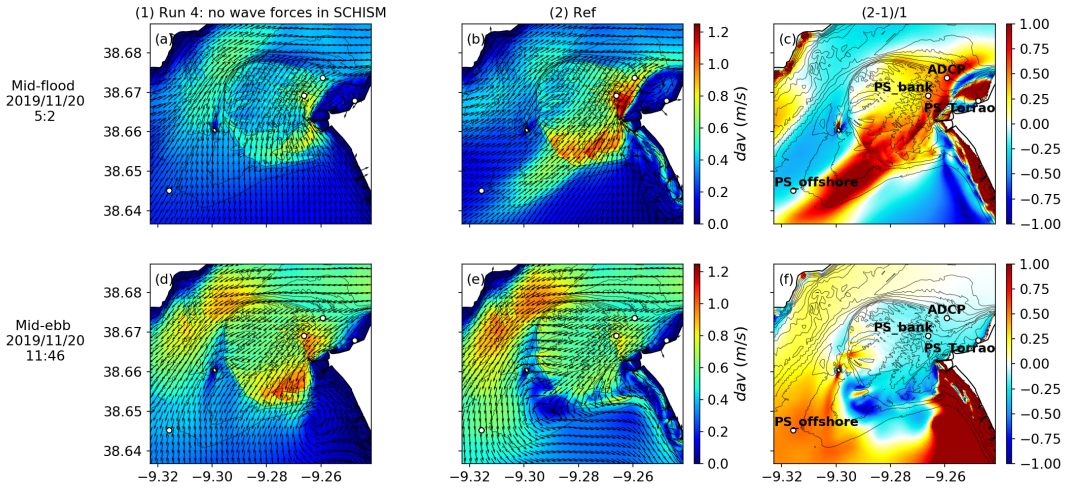

Figure 13. Spatial distributions of depth-averaged currents, *dav* in m/s, at successive mid-flood (MF) and mid-ebb (ME) situations during the storm peak, obtained from simulations (1) *Run 4* [no wave forces in SCHISM] (on **(a)** and **(d)**, respectively) and (2) *Ref* (on **(b)** and **(e)**, respectively). The increasing/decreasing trends of *dav* between *Run 4* and *Ref* at MF and ME ([2-1]/1) are illustrated on **(c)** and **(f)**, respectively.

Depth-averaged velocity fields of two successive MF and ME situations occurring during the peak of the energetic period are compared by accounting (*Ref*) or not (*Run 4*) for wave-induced forces in the circulation model SCHISM (Figure 13).

During flood, currents computed from simulation *Run 4*, that does not include wave-induced forcing, are weak and oriented northward for water depths higher than 7 m at the south of the mouth (Figure 13a). Over the Bugio Bank, they progressively rotate towards the northeast according to the coastline orientation and reach their maximum, around 0.8 m/s, in the secondary flood channel in which the ADCP and PS_bank are located. Flood currents enter the main channel

669 flowing towards the north-east with maximum velocities of 0.6 m/s. In *Ref*, when wave-induced
670 circulations are considered, a noticeable change in the current direction is obtained over most of
671 the estuary mouth, with a mean flow oriented according to the average wave direction, i.e. towards
672 the north-east (Figure 13b). Specific circulations caused by waves can be noticed. Pronounced
673 currents (around 0.6 m/s) develop in the shallow region located between PS_offshore and the
674 southwestern border of the Bugio Bank, which corresponds to the offshore extension of the ebb
675 delta. The model analysis of wave force terms involved in the momentum balance enabled to
676 identify the wave breaking-induced acceleration (WBA) as the main contributor of these wave-
677 induced currents. Indeed, during energetic conditions, the surf zone extends offshore and WBA
678 induces this specific wave-induced circulation. Furthermore, a littoral drift is clearly visible along
679 the Caparica Coast (adjacent beach of the southern margin, Figure 1b), which flows towards the
680 northwest due to the obliquity of waves coming from the southwest (refraction over the Bugio
681 Bank). In the secondary channel and over the southern part of the Bugio Bank, flood currents are
682 significantly increased (+60% on average; Figure 13c) by WBA whereas, simultaneously, the
683 entering flow in the main channel is reduced by 20%.
684 During the ebb, waves coming from the southwest tend to deviate the tidal stream from the main
685 channel southward. Thus, a counterclockwise circulation is generated around the ebb delta in
686 simulation *Ref* (Figure 13e), that is not found in *Run 4* (Figure 13d) where currents remain mainly
687 oriented towards the south-southwest. The circulation influenced by waves in *Ref* exhibits an
688 onshore orientation to the south of the Bugio Bank, and then turns towards the south-east along
689 the 7-m isobath. Over the Bugio Bank, WBA substantially reduces the magnitude of ebb currents,
690 in particular in the secondary channel (-20% on average, up to -50%; Figure 13f). In order to
691 compensate for the influence of this opposed wave-induced circulation, the ebb tidal jet intensifies
692 in the main channel (+20%).
693 It should be reminded that MF and ME situations presented on figure 13 are characterized by
694 intense tidal flows and energetic wave conditions. When H_{m0} at PS_offshore becomes lower than
695 1 m, the contribution of waves to circulations vanishes because waves are too small to break on
696 the ebb shoal (not illustrated).
697 During HT and LT tidal levels, when tidal currents are weak, the entire mouth circulation can be
698 driven by waves. During the storm peak, wave-induced circulation described a band extending
699 from PS_offshore to the ADCP station, with currents ranging from 0.5 and 0.9 m/s (not illustrated
700 here). At the ADCP station, the relevance of wave-induced circulations during energetic conditions
701 is clearly highlighted, with substantial or even dominant contributions to currents between LT and
702 MF levels (Figure 6). Indeed, the wave-induced circulation is more intense at LT over the southern
703 border of the Bugio Bank, due to reduced water depths which promote wave breaking.
704 Lastly, as recently highlighted at the mouth of other inlets (e.g. Akan et al., 2017), wave-induced
705 circulations in turn influence wave fields at the TEM (not illustrated here). In particular, waves
706 tend to reinforce the ebb stream in the main channel, which promotes wave steepening and results
707 in larger H_{m0} (+10%).
708

6. Discussion

6.1. Model predictive skills and limitations

After the arrival of the large swell on the 20/11 (H_{m0} larger than 2 m with T_p over 20 s), wave heights measured at PS_offshore increase by +35% at low tide in comparison with the high tide situation (see low tides of the 20/11 at 3pm and the 21/11 at 3h30am on Figure 3b). The model fails to reproduce this H_{m0} increase during low tide levels associated with energetic conditions, even when currents are considered. At PS_offshore, located at a mean water depth of 10.6 m, changes in water levels between high tide and low tide can only explain small variations of H_{m0} due to shoaling (around 3%). During this type of energetic conditions, satellite images show complex interference wave patterns over the offshore extension of the Bugio Bank (Figure 14), where PS_offshore is located. These observations suggest that wave propagation becomes complex over this region and may result from combined refraction and diffraction processes, which would tend to concentrate the wave energy at some locations, thereby increasing wave heights. The fact that the model fails to reproduce increased H_{m0} at low tide could be explained by the fact that diffraction is not considered here.

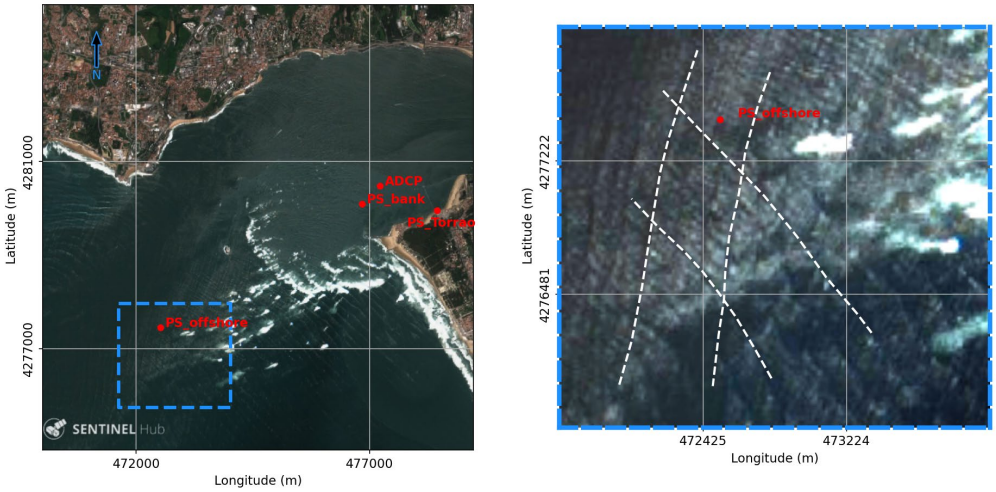

Figure 14. Satellite image (Sentinel mission) at the Tagus Estuary Mouth, the 18th April of 2018, with a zoom provided over the region where the sensor *PS_offshore* is located (dashed white lines depict some wave crests). On this date, offshore conditions at the Nazaré Buoy (location on Figure 1a) were energetic and close to those associated with the

storm peak of the present field campaign, with H_{m0} of 6 m, T_p of 17.5 s and a *Mwd* of 295°N. Note that no satellite image was available during the storm peak due to the presence of clouds.

The comparison between observed and modelled PSD at low tide (Figure 9) showed triad interactions promote substantial energy transfers from the spectral peak to higher harmonics. However, in more details, energy is accurately transferred to the second ($2\times f_p$) but not to the third ($3\times f_p$) harmonic. This problem is inherent to the Lumped Triad Approximation of Eldeberky (1996) (Booij et al., 2009) and could partly explain why the model slightly underestimates the tidal modulation of T_{m02}. Moreover, the performance of the LTA is not optimal on complex bathymetries, such as in barred beaches (Mendes et al., 2018), and more research is needed to adequately account for triads in phase-averaged wave models.

The model also underestimates the energy reduction associated with high frequencies during ebb. In addition, the tidal modulation of T_{m02} at PS_bank or PS_Torrao, which generally shows that T_{m02} increases during the ebb, is weaker than in the observations,. As ebb currents over the ebb delta can reach 1 m/s, we hypothesize that the drop of wave energy in the high frequency part of wave spectra observed along the coast during the ebb (e.g. Figure 10) is due to dissipation by whitecapping, as proposed in previous studies (e.g. Westhuysen et al., 2007; Ardhuin et al., 2010; Westhuysen, 2012; Dodet et al., 2013). In an additional simulation (*Run 5*), an adaptive saturation threshold B_r was considered in the original formulation of Ardhuin et al. (2010), assuming an exponential decrease of the latter for f>0.2 Hz (HF). As illustrated on Figure 10b, the reduced B_r values for HF result in sharper reductions of the wave energy during the ebb at PS_Torrao, in agreement with observations. Therefore, it may mean that, based on the original formulation that considers a constant B_r, the saturation level is close but just below this threshold above which the whitecapping is activated (i.e. critical steepening). Since other studies provided evidence for overestimations of wave energy associated with high frequencies under moderate to intense current conditions (e.g. Bennis et al., 2020), specific attention should be paid to the whitecapping dissipation in future studies.

In future research, more attention should be paid to non-linear interactions occurring when waves face intense countercurrents. Countercurrents promote wave steepening and subsequent dissipation by breaking, but also induce resonant interactions that strongly affect the non-linear evolution of waves, which results in substantial energy transfers and frequency downshift (e.g. Shugan et al., 2015). Therefore, in addition to the possible inadequate formulation of the saturation threshold for whitecapping discussed above, the fact that these resonant interactions are not represented in spectral wave models could locally explain the discrepancies between wave spectra modelled and derived from field observations. In addition, the wave action equation solved by spectral wave models is not fully valid in areas such as the TEM, since it was derived for waves propagating in “slowly varying media” (Bretherton and Garrett, 1968). Hence, other approaches should probably be used to investigate these processes in detail.

6.2. New insights on wave-current interactions

Despite the potential limitation of the model regarding energy dissipation by whitecapping (section 6.1), a substantial part of wave modulations was identified to be driven by current-induced refraction over some regions of the TEM characterized by weak local circulations (including PS_Torrao). According to model results, this effect of currents on the propagation of waves locally contributes to 20-30% of the tidal modulation of wave heights, while tidal ranges were medium, suggesting larger values under spring tides. Flood currents enhance refraction and induce a clockwise rotation of waves by 10-15°, thereby focusing more wave energy towards the southern margin of the mouth, while ebb currents produce an opposite effect by reducing the energy reaching the coast. To our knowledge, such an effect of currents on the tidal modulation of waves has never been described before. In addition to well-known current effects on waves propagation and dissipation (e.g. review of Wolf and Prandle, 1999), recent knowledge on wave-current interactions at the mouth of inlet systems mainly concerned wave focusing (e.g. Olabarrieta et al., 2011 ; Dodet et al., 2013 ; Akan et al., 2017) and steepening due to opposing currents during the ebb (e.g. Rusu et al., 2011 ; Elias et al., 2012; Dodet et al., 2013; Jia et al., 2015; Akan et al., 2017), and subsequent dissipation by whitecapping (e.g. Westhuysen, 2012). This study highlights that wave modulations due to current-induced refraction, a process previously identified between islands or on the inner shelf (e.g. Hopkins et al., 2006; Ardhuin et al., 2012), can also be relevant at the mouth of large estuaries.

Besides, the literature on wave-induced circulations is mostly restricted to small and medium-size inlet systems (e.g. Bertin et al., 2009; Olabarrieta et al., 2011; Wargula et al., 2014; Chen et al., 2015; Akan et al., 2017), while their contribution in case of large estuaries remains mostly unexplored. Yet, Fortunato et al. (2017) showed that onshore directed waves forces resulting from wave breaking over the Tagus Ebb Delta could generate wave-induced setup reaching tens of centimeters inside the estuary during extreme events (1941 storm with offshore significant wave heights of 14 m). The present study further revealed that storm waves can also substantially impact the mean circulation, even at the scale of a wide and deep estuary mouth. Qualitatively, some similarities can be underlined with smaller inlet systems regarding circulation patterns (e.g. Olabarrieta et al., 2011; Orescanin et al., 2014; Chen et al., 2015; Akan et al., 2017), although the impact of short wave breaking is more pronounced in this study, especially in secondary channels (locally increased by a factor 3). In addition, according to Fortunato et al. (2017), the return period of the storm waves considered in this study is less than one year, with several occurrences during each winter. By considering extreme events with return periods of 10 years (offshore significant wave height $H_s \approx 10$ m) or 100 years ($H_s \approx 15$ m), we could expect that wave-induced circulations would substantially intensify and become fully dominant.

7. Conclusions and perspectives

Interactions between waves, currents and water levels have been assessed at the mouth of the Tagus Estuary (the second largest estuary in Europe) during storm wave conditions, by combining field observations and the application of a 3D fully-coupled wave-current modelling system. Three pressure sensors and one ADCP were deployed across the ebb delta at water depths ranging from 3 to 11 m. Wave-current interactions were firstly investigated at measurement stations, which enabled to ensure the model validity in terms of both waves and currents. Series of numerical simulations were performed over the entire estuary mouth in order to discriminate the effects of water levels and currents on wave fields on the one hand, and the influence of waves on circulations at different tidal phases on the other hand. The main conclusions and perspectives from this work are:

- As already reported at the mouth of other inlet systems, the combination between bathymetric features associated with the shallow ebb delta region and the mesotidal forcing plays a key role in the modulation of waves. During energetic conditions, low tide levels promote depth-limited wave breaking over the ebb shoal, which results in reduced wave heights shoreward (by 50% to more than 100% depending on the location).
- Triad wave interactions associated with wave non-linearity developing by shallow water depth promote energy transfers from the spectral peaks to higher harmonics and thereby explain the observed decrease of the mean wave period T_{m02} as the water depth is reduced. In more details, the LTA approach used in this study fails to transfer energy to the third harmonic, which partly explains why the model underestimates the drop of T_{m02} at low tide. More advanced approaches for triad modelling (e.g. Salmon et al., 2016) will have to be considered to see if they better predict energy transfers with complex sea states as in the TEM.
- At the mouth, current-induced refraction appears as a major process explaining a substantial part of the modulation of wave heights (20-30%), never described in case of a large estuary. Flood currents change the mean wave direction by 10-15° and tend to concentrate the wave energy towards coastal regions of the southern margin, while an opposite effect is induced by ebb currents. On the contrary, in the deep main channel, ebb currents opposed to wave direction focus the wave energy through refraction and promote wave shoaling (H_{m0} increased by 20%).
- Regarding the current effect on wave dissipation over some regions of the ebb shoal, model-data comparison suggests that the saturation level is close but just below the threshold above which whitecapping starts to occur and that further developments are needed to better model wave dissipation in such conditions.
- During energetic conditions, wave breaking-induced acceleration occurring over the ebb shoal substantially influences both the orientation and the magnitude of circulations at the estuary mouth and along adjacent coasts. Wave forces enhance (resp. reduce) tidal currents by 50 to 300% over the ebb shoal during the flood (resp. the ebb), leading to a relative

decrease (resp. increase) of 25% of the tidal flow in the deep main channel. However, due to a malicious act, no current measurements were available under energetic wave conditions and these findings presently rely on modeling results. Although very challenging, future field campaigns will have to be carried out at the mouth of large estuary mouths under storm waves.

- The influence of waves on circulations in turn affects wave fields, e.g. enhanced H_{m0} increase at the main channel entrance during the ebb, demonstrating the complexity of interactions between waves and currents, and the interest of considering a fully coupled wave-current model.

This study highlighted that complex interactions between waves and tidal currents can occur at the mouth of a large estuary, including substantial modulations of waves heights caused by current-induced refraction and intense wave-induced circulations. Further research should be dedicated to extreme wave events, which appear challenging for both data acquisitions and numerical modelling.

Acknowledgments

This study was funded by the Fondation de France and Fondation Edouard et Geneviève Buffard. Authors greatly acknowledge other contributors involved in the collaborative project "*Nouveaux Commanditaires Science*", including Livio Riboli-Sasco (project mediator; Atelier des Jours à Venir), João Cão (Center for Philosophy of Sciences, University of Lisbon) and Tatiana Arquizan (Canto do Curió Cultural Association, Lisbon), who initiated and managed the project in collaboration with local populations. Inhabitants from Segundo Torrão and Cova do Vapor are deeply thanked for their support on the field, especially the fisherman Toni Graça who provided a boat and his site experience during field campaigns. Bathymetric data were obtained under the COSMO Programme - Coastal Monitoring Programme of Continental Portugal, of the Portuguese Environment Agency, co-funded by the Operational Program for Sustainability and Efficiency in the Use of Resources (POSEUR). These data were downloaded on April 2019 from https://cosmo.apambiente.pt. Lastly, XB, ABF and DM were supported by the INLEX project, funded by the French ANR and the Portuguese FCT (project 40791ZC).

Appendix A. Solving the wave dispersion relation with current effect

Energy density spectra (PSD) obtained from pressure measurements by applying Fast Fourier Transforms need to be converted in elevation spectra *E(f)*. A Transfer Function Method based on the linear wave theory (e.g. Bishop and Donelan, 1987) is used at each frequency *f* such as

$$E(f) = \frac{PSD(f)}{K_p(f)^2} \quad \text{(A.1)}$$

and

$$K_p(f) = \frac{\cosh(k(f)h_{sensor})}{\cosh(k(f)h)} \quad \text{(A.2)}$$

where h_{sensor} is the sensor height above the bottom, h is the water depth, and k is the wave number computed from the linear wave theory. The dispersion relation from the linear wave theory reads

$$\sigma^2 = gk\tanh(kh) \quad \text{(A.3)}$$

where σ is the relative angular frequency. In the presence of intense currents, k can be substantially modulated and thus requires a correction to ensure the relevance of elevation spectra. First, the wave number k has to be computed without current-wave interaction. The logarithmic matching method of Guo (2002) has been applied to Eq. (A.3) as follows

$$k = \frac{{\omega_a}^2}{h(1-e^{-\omega_a{}^{\beta}})^{-1/\beta}} \quad \text{(A.4)}$$

with

$$\omega_a = \frac{\omega}{\sqrt{g/h}} \quad \text{(A.5)}$$

where ω is the absolute angular frequency (=$2\pi f$; in rad/s), g is the gravitational acceleration, and β is a shape parameter set at 2.4908.

According to Sanchez (2012), a wave number accounting for the current, $k_{cur,0}$, can be computed as

$$k_{cur,0} = 0.3k + \frac{0.7(\omega - kU)^2}{g\tanh(kh)} \quad \text{(A.6)}$$

where U is the current velocity in the wave direction. Finally, a Newton-Raphson iterative method (10 iterations considered here; Eq. A.7) is applied to improve the accuracy of the final solution by defining the initial k value, $k_{i=0}$, as $k_{cur,0}$.

$$k_{i+1} = k_i - \frac{gk_i\tanh(k_ih) - (\omega - k_iU)^2}{g\left(\tanh(k_ih) - k_ih(\tanh(k_ih)^2 - 1)\right) + 2U(\omega - k_iU)} \quad \text{(A.7)}$$

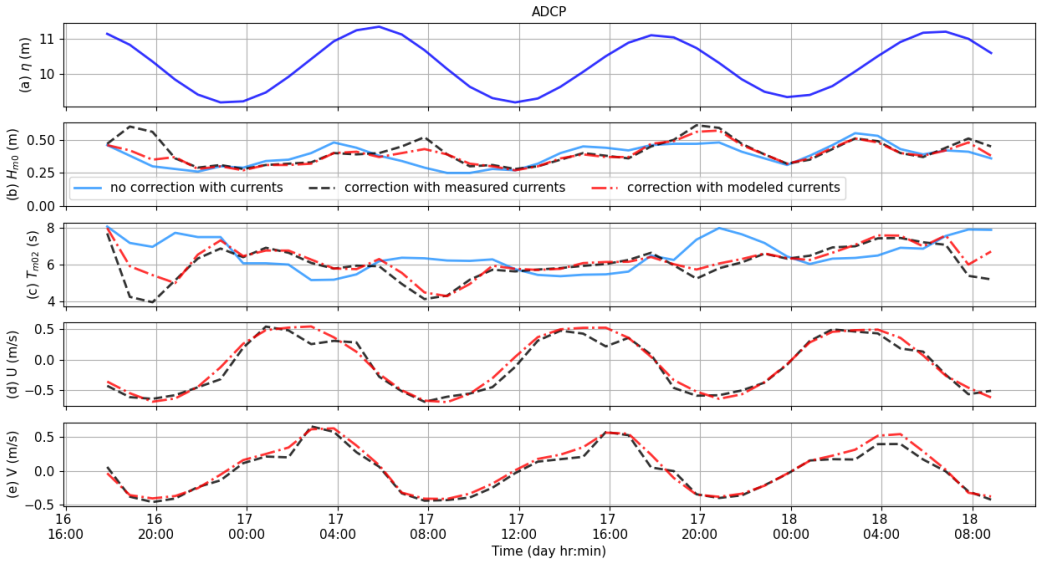

Figure A1. (a) Water elevations measured at the ADCP station (see location on Figure 1b). Temporal series of H_{m0} **(b)** and T_{m02} **(c)** obtained without current effect (solid line), or by including measured (dashed line) or modelled (dashed-dotted line) currents in the wave dispersion relation, with the corresponding zonal (U) and meridional (V) components of currents illustrated on **(d)** and **(e)**, respectively.

Pressure measurements from the ADCP have been processed by considering 20-minute-long bursts, corrected from atmospheric pressure and detrended. The effect of tidal currents on the reconstitution of elevation spectra is investigated through comparisons on wave bulk parameters H_{m0} and T_{m02} (see more details on their computation in section 2.2), as illustrated on Figure A1. The current effect becomes substantial during the flood and the ebb, when currents reach their maximum. As expected, flood currents tend to reduce H_{m0} and increase T_{m02}, while ebb currents have opposite effects. Consistent corrections are obtained by considering currents from the ADCP or from the model, which underlines the relevance of the latter regarding hydrodynamics.

Given their substantial impact on the modulation of mean wave parameters, tidal currents are included in the processing of pressure measurements at all stations, with a similar procedure than the one used by de Wit et al. (2019). Indeed, tidal currents provided by the model are used at the other measuring stations where current measurements are unfortunately not available, given its ability in describing tidal-induced circulations at the Tagus Estuary Mouth.

References

Akan, Ç., Moghimi, S., Özkan-Haller, H.T., Osborne, J., Kurapov, A., 2017. On the dynamics of the Mouth of the Columbia River: Results from a three-dimensional fully coupled wave-current interaction model. Journal of Geophysical Research: Oceans 122, 5218–5236. https://doi.org/10.1002/2016JC012307

Andrews, Dg., McIntyre, M.E., 1978. An exact theory of nonlinear waves on a Lagrangian-mean flow. Journal of fluid Mechanics 89, 609–646.

Ardhuin, F., Jenkins, A.D., 2006. On the Interaction of Surface Waves and Upper Ocean Turbulence. J. Phys. Oceanogr. 36, 551–557. https://doi.org/10.1175/JPO2862.1

Ardhuin, F., Marié, L., Rascle, N., Forget, P., Roland, A., 2009. Observation and Estimation of Lagrangian, Stokes, and Eulerian Currents Induced by Wind and Waves at the Sea Surface. J. Phys. Oceanogr. 39, 2820–2838. https://doi.org/10.1175/2009JPO4169.1

Ardhuin, F., Rascle, N., Belibassakis, K.A., 2008. Explicit wave-averaged primitive equations using a generalized Lagrangian mean. Ocean Modelling 20, 35–60. https://doi.org/10.1016/j.ocemod.2007.07.001

Ardhuin, F., Rogers, E., Babanin, A.V., Filipot, J.-F., Magne, R., Roland, A., van der Westhuysen, A., Queffeulou, P., Lefevre, J.-M., Aouf, L., Collard, F., 2010. Semiempirical Dissipation Source Functions for Ocean Waves. Part I: Definition, Calibration, and Validation. J. Phys. Oceanogr. 40, 1917–1941. https://doi.org/10.1175/2010JPO4324.1

Ardhuin, F., Roland, A., Dumas, F., Bennis, A.-C., Sentchev, A., Forget, P., Wolf, J., Girard, F., Osuna, P., Benoit, M., 2012. Numerical Wave Modeling in Conditions with Strong Currents: Dissipation, Refraction, and Relative Wind. J. Phys. Oceanogr. 42, 2101–2120. https://doi.org/10.1175/JPO-D-11-0220.1

Baldock, T.E., Holmes, P., Bunker, S., Van Weert, P., 1998. Cross-shore hydrodynamics within an unsaturated surf zone. Coastal Engineering 34, 173–196. https://doi.org/10.1016/S0378-3839(98)00017-9

Beji, S., Battjes, J.A., 1993. Experimental investigation of wave propagation over a bar. Coastal Engineering 19, 151–162.

Bendat, J.S., Piersol, A.G., 1971. Random Data Analysis and Measurement Procedures, John Wiley&Sons. ed.

Bennis, A.-C., Ardhuin, F., Dumas, F., 2011. On the coupling of wave and three-dimensional circulation models: Choice of theoretical framework, practical implementation and adiabatic tests. Ocean Modelling 40, 260–272. https://doi.org/10.1016/j.ocemod.2011.09.003

Bennis, A.-C., Furgerot, L., Bailly Du Bois, P., Dumas, F., Odaka, T., Lathuilière, C., Filipot, J.-F., 2020. Numerical modelling of three-dimensional wave-current interactions in complex environment: Application to Alderney Race. Applied Ocean Research 95, 102021. https://doi.org/10.1016/j.apor.2019.102021

Bertin, X., Fortunato, A.B., Oliveira, A., 2009. Morphodynamic Modeling of the Ancão Inlet, South Portugal. Journal of Coastal Research 10–14.

Bertin, X., Li, K., Roland, A., Bidlot, J.-R., 2015. The contribution of short-waves in storm surges: Two case studies in the Bay of Biscay. Continental Shelf Research 96, 1–15.

Bertin, X., Mendes, D., Martins, K., Fortunato, A.B., Lavaud, L., 2019. The closure of a shallow tidal inlet promoted by infragravity waves. Geophysical Research Letters 46, 6804–6810.

Bishop, C.T., Donelan, M.A., 1987. Measuring waves with pressure transducers. Coastal Engineering 11, 309–328.

Bolaños, R., Brown, J.M., Souza, A.J., 2014. Wave–current interactions in a tide dominated estuary. Continental Shelf Research 87, 109–123.

Booij, N., Holthuijsen, L.H., Bénit, M.P., 2009. A distributed collinear triad approximation in SWAN, in: Proceedings Of Coastal Dynamics 2009: Impacts of Human Activities on Dynamic Coastal Processes. World Scientific, pp. 1–10.

Bretherton, F. P., Garrett C. J. R., 1968. Wavetrains in inhomogeneous moving media. Proc. R. Soc. London A 302(1471), 529–554.

Cavaleri, L., Abdalla, S., Benetazzo, A., Bertotti, L., Bidlot, J.-R., Breivik, Ø., Carniel, S., Jensen, R.E., Portilla-Yandun, J., Rogers, W.E., Roland, A., Sanchez-Arcilla, A., Smith, J.M., Staneva, J., Toledo, Y., van Vledder, G.Ph., van der Westhuysen, A.J., 2018. Wave modelling in coastal and inner seas. Progress in Oceanography 167, 164–233. https://doi.org/10.1016/j.pocean.2018.03.010

Chawla, A., Kirby, J.T., 2002. Monochromatic and random wave breaking at blocking points. Journal of Geophysical Research: Oceans 107, 4–1.

Chen, H., Zou, Q., 2018. Characteristics of wave breaking and blocking by spatially varying opposing currents. Journal of Geophysical Research: Oceans 123, 3761–3785.

Chen, J.-L., Hsu, T.-J., Shi, F., Raubenheimer, B., Elgar, S., 2015. Hydrodynamic and sediment transport modeling of New River Inlet (NC) under the interaction of tides and waves. Journal of Geophysical Research: Oceans 120, 4028–4047. https://doi.org/10.1002/2014JC010425

Chen, Y., Chen, L., Zhang, H., Gong, W., 2019. Effects of wave-current interaction on the Pearl River Estuary during Typhoon Hato. Estuarine, Coastal and Shelf Science 228, 106364.

Costa, M.J., Vasconcelos, R., Costa, J.L., Cabral, H.N., 2007. River flow influence on the fish community of the Tagus estuary (Portugal). Hydrobiologia 587, 113–123.

de Wit, F., Tissier, M., Reniers, A., 2019. Characterizing Wave Shape Evolution on an Ebb-Tidal Shoal. Journal of Marine Science and Engineering 7, 367. https://doi.org/10.3390/jmse7100367

Delpey, M.T., Ardhuin, F., Otheguy, P., Jouon, A., 2014. Effects of waves on coastal water dispersion in a small estuarine bay. Journal of Geophysical Research: Oceans 119, 70–86.

Dodet, G., Bertin, X., Bruneau, N., Fortunato, A.B., Nahon, A., Roland, A., 2013. Wave-current interactions in a wave-dominated tidal inlet. Journal of Geophysical Research: Oceans 118, 1587–1605.

Dodet, G., Bertin, X., Taborda, R., 2010. Wave climate variability in the North-East Atlantic Ocean over the last six decades. Ocean Modelling 31, 120–131. https://doi.org/10.1016/j.ocemod.2009.10.010

Eldeberky, Y., 1996. Nonlinear transformation of wave spectra in the nearshore. Delft University of Technology, Delft, Netherlands.

Elgar, S., 1987. Bias of effective degrees of freedom of a spectrum. Journal of Waterway, Port, Coastal, and Ocean Engineering 113, 77–82.

Elgar, S., Guza, R.T., 1985. Observations of bispectra of shoaling surface gravity waves. Journal of Fluid Mechanics 161, 425–448.

Elias, E.P.L., Gelfenbaum, G., Westhuysen, A.J.V. der, 2012. Validation of a coupled wave-flow model in a high-energy setting: The mouth of the Columbia River. Journal of Geophysical Research: Oceans 117. https://doi.org/10.1029/2012JC008105

Feddersen, F., 2012. Scaling surf zone turbulence. Geophysical Research Letters 39.

Fortunato, A., Oliveira, A., Baptista, A.M., 1999. On the effect of tidal flats on the hydrodynamics of the Tagus estuary. Oceanologica Acta 22, 31–44. https://doi.org/10.1016/S0399-1784(99)80030-9

Fortunato, A.B., Freire, P., Bertin, X., Rodrigues, M., Ferreira, J., Liberato, M.L.R., 2017. A numerical study of the February 15, 1941 storm in the Tagus estuary. Continental Shelf Research 144, 50–64. https://doi.org/10.1016/j.csr.2017.06.023

Fortunato, A.B., Freire, P., Mengual, B., Bertin, X., Pinto, C., Martins, K., Guérin, T., Azevedo, A., 2021. Sediment dynamics and morphological evolution in the Tagus Estuary inlet. Marine Geology 440, 106590. https://doi.org/10.1016/j.margeo.2021.106590

Freire, P., Taborda, R., Silva, A.M., 2007. Sedimentary characterization of Tagus estuarine beaches (Portugal). J Soils Sediments 7, 296–302. https://doi.org/10.1065/jss2007.08.243

Guérin, T., Bertin, X., Coulombier, T., de Bakker, A., 2018. Impacts of wave-induced circulation in the surf zone on wave setup. Ocean Modelling 123, 86–97.

Guerreiro, M., Fortunato, A.B., Freire, P., Rilo, A., Taborda, R., Freitas, M.C., Andrade, C., Silva, T., Rodrigues, M., Bertin, X., 2015. Evolution of the hydrodynamics of the Tagus estuary (Portugal) in the 21st century. Revista de Gestão Costeira Integrada-Journal of Integrated Coastal Zone Management 15, 65–80.

Guo, J., 2002. Simple and explicit solution of wave dispersion equation. Coastal Engineering 45, 71–74.

Hasselmann, K., Barnett, T.P., Bouws, E., Carlson, H., Cartwright, D.E., Enke, K., Ewing, J.A., Gienapp, H., Hasselmann, D.E., Kruseman, P., Meerburg, A., Müller, P., Olbers, D.J., Richter, K., Sell, W., Walden, H., 1973. Measurements of wind-wave growth and swell decay during the Joint North Sea Wave Project (JONSWAP). Deutches Hydrographisches Institut, Hydraulic Engineering Reports 8, 95–102.

Hasselmann, S., Hasselmann, K., Allender, J.H., Barnett, T.P., 1985. Computations and parameterizations of the nonlinear energy transfer in a gravity-wave specturm. Part II: Parameterizations of the nonlinear energy transfer for application in wave models. Journal of Physical Oceanography 15, 1378–1391.

Herbers, T.H.C., Russnogle, N.R., Elgar, S., 2000. Spectral Energy Balance of Breaking Waves within the Surf Zone. J. Phys. Oceanogr. 30, 2723–2737. https://doi.org/10.1175/1520-0485(2000)030<2723:SEBOBW>2.0.CO;2

Holthuijsen, L.H., Tolman, H.L., 1991. Effects of the Gulf Stream on ocean waves. Journal of Geophysical Research: Oceans 96, 12755–12771.

Hopkins, J., Elgar, S., Raubenheimer, B., 2016. Observations and model simulations of wave-current interaction on the inner shelf. Journal of Geophysical Research: Oceans 121, 198–208.

Inch, K., Davidson, M., Masselink, G., Russell, P., 2017. Observations of nearshore infragravity wave dynamics under high energy swell and wind-wave conditions. Continental Shelf Research 138, 19–31.

Irvine, D., 1987. Extreme waves in the Agulhas- A case study in wave-current interaction. Johns Hopkins APL Technical Digest 8, 100–106.

Janssen, T.T., Battjes, J.A., 2007. A note on wave energy dissipation over steep beaches. Coastal Engineering 54, 711–716. https://doi.org/10.1016/j.coastaleng.2007.05.006

Jia, L., Wen, Y., Pan, S., Liu, J.T., He, J., 2015. Wave–current interaction in a river and wave dominant estuary: A seasonal contrast. Applied Ocean Research 52, 151–166. https://doi.org/10.1016/j.apor.2015.06.004

Kang, K., Di Iorio, D., 2006. Depth- and current-induced effects on wave propagation into the Altamaha River Estuary, Georgia. Estuarine, Coastal and Shelf Science 66, 395–408. https://doi.org/10.1016/j.ecss.2005.09.008

Kirby, J.T., Chen, T.-M., 1989. Surface waves on vertically sheared flows: approximate dispersion relations. Journal of Geophysical Research: Oceans 94, 1013–1027.

Komen, G.J., Cavaleri, L., Donelan, M., Hasselmann, K., Hasselmann, S., Janssen, P.A.E.M., 1996. Dynamics and Modelling of Ocean Waves, Cambridge Univ. Press. ed. Cambridge, U.K.

Kudryavtsev, V.N., Grodsky, S.A., Dulov, V.A., Bol'Shakov, A.N., 1995. Observations of wind waves in the Gulf Stream frontal zone. Journal of Geophysical Research: Oceans 100, 20715–20727.

Kumar, N., Voulgaris, G., Warner, J.C., Olabarrieta, M., 2012. Implementation of the vortex force formalism in the coupled ocean-atmosphere-wave-sediment transport (COAWST) modeling system for inner shelf and surf zone applications. Ocean Modelling 47, 65–95.

Lavrenov, I.V., 1998. The wave energy concentration at the Agulhas current off South Africa. Natural hazards 17, 117–127.

Lin, S., Sheng, J., Ohashi, K., Song, Q., 2021. Wave-current interactions during Hurricanes Earl and Igor in the northwest Atlantic. Journal of Geophysical Research: Oceans e2021JC017609.

Lyard, F.H., Allain, D.J., Cancet, M., Carrère, L., Picot, N., 2021. FES2014 global ocean tide atlas: design and performance. Ocean Science 17, 615–649.

Mellor, G., 2003. The Three-Dimensional Current and Surface Wave Equations. J. Phys. Oceanogr. 33, 1978–1989. https://doi.org/10.1175/1520-0485(2003)033<1978:TTCASW>2.0.CO;2

Mendes, D., Fortunato, A.B., Bertin, X., Martins, K., Lavaud, L., Nobre Silva, A., Pires-Silva, A.A., Coulombier, T., Pinto, J.P., 2020. Importance of infragravity waves in a wave-dominated inlet under storm conditions. Continental Shelf Research 192, 104026. https://doi.org/10.1016/j.csr.2019.104026

Mendes, D., Oliveira, T.C.A., 2021. Deep-water spectral wave steepness offshore mainland Portugal. Ocean Engineering 236, 109548. https://doi.org/10.1016/j.oceaneng.2021.109548

Mendes, D., Pinto, J.P., Pires-Silva, A.A., Fortunato, A.B., 2018. Infragravity wave energy changes on a dissipative barred beach: A numerical study. Coastal Engineering 140, 136–146. https://doi.org/10.1016/j.coastaleng.2018.07.005

Moghimi, S., Klingbeil, K., Gräwe, U., Burchard, H., 2013. A direct comparison of a depth-dependent Radiation stress formulation and a Vortex force formulation within a three-dimensional coastal ocean model. Ocean Modelling, Ocean Surface Waves 70, 132–144. https://doi.org/10.1016/j.ocemod.2012.10.002

Neves, F. dos S., 2010. Dynamics and hydrology of the Tagus estuary: results from in situ observations. University of Lisbon, Portugal.

Oh, J.-E., Jeong, W.-M., Chang, Y.S., Oh, S.-H., 2020. On the Separation Period Discriminating Gravity and Infragravity Waves off Gyeongpo Beach, Korea. Journal of Marine Science and Engineering 8, 167. https://doi.org/10.3390/jmse8030167

Olabarrieta, M., Warner, J.C., Kumar, N., 2011. Wave-current interaction in Willapa Bay. Journal of Geophysical Research: Oceans 116.

Orescanin, M., Raubenheimer, B., Elgar, S., 2014. Observations of wave effects on inlet circulation. Continental Shelf Research 82, 37–42.

Phillips, O.M., 1977. The dynamics of the upper ocean. Cambrige Univ.

Pond, S., Pickard, G.L., 1998. Introductory Dynamical Oceanography. Gulf Professional Publishing.

Rodi, W., 1993. Turbulence Models and Their Application in Hydraulics. IAHR Monograph: Delft, Delft, Netherlands.

Rodrigues, M., Fortunato, A.B., 2017. Assessment of a three-dimensional baroclinic circulation model of the Tagus estuary (Portugal). AIMS Environ. Sci 4, 763–787.

Roelvink, J.A., Stive, M.J.F., 1989. Bar-generating cross-shore flow mechanisms on a beach. Journal of Geophysical Research: Oceans 94, 4785–4800.

Roland, A., Zhang, Y.J., Wang, H.V., Meng, Y., Teng, Y.-C., Maderich, V., Brovchenko, I., Dutour-Sikiric, M., Zanke, U., 2012. A fully coupled 3D wave-current interaction model on unstructured grids. Journal of Geophysical Research: Oceans 117.

Ruessink, B.G., Walstra, D.J.R., Southgate, H.N., 2003. Calibration and verification of a parametric wave model on barred beaches. Coastal Engineering 48, 139–149. https://doi.org/10.1016/S0378-3839(03)00023-1

Rusu, E., Soares, C.G., 2011. Wave modelling at the entrance of ports. Ocean Engineering 38, 2089–2109.

Rusu, L., Bernardino, M., Soares, C.G., 2011. Modelling the influence of currents on wave propagation at the entrance of the Tagus estuary. Ocean Engineering 38, 1174–1183.

Saha, S., Moorthi, S., Wu, X., Wang, J., Nadiga, S., Tripp, P., Behringer, D., Hou, Y.-T., Chuang, H., Iredell, M., Ek, M., Meng, J., Yang, R., Mendez, M.P., van den Dool, H., Zhang, Q., Wang, W., Chen, M., Becker, E., 2014. The NCEP Climate Forecast System Version 2. J. Climate 27, 2185–2208. https://doi.org/10.1175/JCLI-D-12-00823.1

Salgueiro, A.R., Machado, M.J., Barriendos, M., Pereira, H.G., Benito, G., 2013. Flood magnitudes in the Tagus River (Iberian Peninsula) and its stochastic relationship with daily North Atlantic Oscillation since mid-19th Century. Journal of hydrology 502, 191–201.

Salmon, J.E., Smit, P.B., Janssen, T.T., Holthuijsen, L.H., 2016. A consistent collinear triad approximation for operational wave models. Ocean Modelling 104, 203–212.

Sanchez, A., 2012. wavenumber.m. MATLAB Central File Exchange.

Shugan, I.V., Hwung, H.H., Yang, R.Y., 2015. An analytical model of the evolution of a Stokes wave and its two Benjamin–Feir sidebands on nonuniform unidirectional current. Nonlinear Processes in Geophysics 22, 313–324.

Smith, S.J., Smith, J.M., 2001. Numerical modeling of waves at Ponce de Leon Inlet, Florida. Journal of waterway, port, coastal, and ocean engineering 127, 176–184.

Song, Y., Haidvogel, D., 1994. A Semi-implicit Ocean Circulation Model Using a Generalized Topography-Following Coordinate System. Journal of Computational Physics 115, 228–244. https://doi.org/10.1006/jcph.1994.1189

Soulsby, R., 1997. Dynamics of marine sands: a manual for practical applications. Thomas Telford.

Terray, E.A., Donelan, M.A., Agrawal, Y.C., Drennan, W.M., Kahma, K.K., Williams, A.J., Hwang, P.A., Kitaigorodskii, S.A., 1996. Estimates of kinetic energy dissipation under breaking waves. Journal of Physical Oceanography 26, 792–807.

The WAVEWATCH III Development Group (WW3DG), 2019. User manual and system documentation of WAVEWATCH III version 6.07. Tech. Note 333, NOAA/NWS/NCEP/MMAB, College Park, MD, USA, 465 pp. + Appendices.

Uchiyama, Y., McWilliams, J.C., Shchepetkin, A.F., 2010. Wave–current interaction in an oceanic circulation model with a vortex-force formalism: Application to the surf zone. Ocean Modelling 34, 16–35.

Umlauf, L., Burchard, H., 2003. A generic length-scale equation for geophysical turbulence models. Journal of Marine Research 61, 235–265. https://doi.org/10.1357/002224003322005087

van der Westhuysen, A.J., 2012. Spectral modeling of wave dissipation on negative current gradients. Coastal Engineering 68, 17–30.

van der Westhuysen, A.J., Zijlema, M., Battjes, J.A., 2007. Nonlinear saturation-based whitecapping dissipation in SWAN for deep and shallow water. Coastal Engineering 54, 151–170.

Wargula, A., Raubenheimer, B., Elgar, S., 2014. Wave-driven along-channel subtidal flows in a well-mixed ocean inlet. Journal of Geophysical Research: Oceans 119, 2987–3001. https://doi.org/10.1002/2014JC009839

Wolf, J., Prandle, D., 1999. Some observations of wave–current interaction. Coastal Engineering 37, 471–485.

Zhang, Y., Baptista, A.M., 2008. SELFE: A semi-implicit Eulerian–Lagrangian finite-element model for cross-scale ocean circulation. Ocean Modelling 21, 71–96. https://doi.org/10.1016/j.ocemod.2007.11.005

Zhang, Y.J., Ye, F., Stanev, E.V., Grashorn, S., 2016. Seamless cross-scale modeling with SCHISM. Ocean Modelling 102, 64–81. https://doi.org/10.1016/j.ocemod.2016.05.002

Zippel, S., Thomson, J., 2017. Surface wave breaking over sheared currents: Observations from the M outh of the C olumbia R iver. Journal of Geophysical Research: Oceans 122, 3311–3328.

Highlights:

- Wave-current interactions at a large estuary mouth are analyzed under storm waves
- Refraction of waves by currents explains up to 30% of the modulation of wave heights
- Wave-breaking acceleration is a major driver of the circulation at the mouth scale

Baptiste Mengual : Conceptualization, Methodology, Software, Writing – Original Draft ; **Xavier Bertin** : Conceptualization, Methodology, Writing – Review & Editing, Supervision ; **Florian Place** : Conceptualization, Methodology – Review & Editing ; **Marc Pezerat** : Methodology, Software, Writing – Review & Editing ; **Thibault Coulombier** : Methodology, Writing – Review & Editing ; **Diogo Mendes** : Conceptualization, Methodology, Writing – Review & Editing ; **André Bustorff Fortunato** : Conceptualization, Methodology, Writing – Review & Editing.

Declaration of interests

☒ The authors declare that they have no known competing financial interests or personal relationships that could have appeared to influence the work reported in this paper.

☐ The authors declare the following financial interests/personal relationships which may be considered as potential competing interests: